16

HgCdTe Heterostructures Grown by MBE on Si(310) for Infrared Photodetectors

Maxim Yakushev et al.*
A.V. Rzhanov Institute of Semiconductor Physics
Siberian branch of the RAS
Russian Federation

1. Introduction

A high spatial resolution of infrared (IR) thermal-imaging systems is determined by the amount of pixels of the IR focal plane array (FPA), an increase in which leads to an increase in FPA sizes. To realize such IRFPAs based on mercury cadmium telluride (MCT) alloys, a photosensitive material with a high lateral uniformity of the composition is required. Recently, considerable effort has been directed to the development of the growth of heteroepitaxial MCT structures by molecular beam epitaxy (MBE) on Si large in diameter substrates [Reddy et al., 2008].

Matrix IR FPAs are produced by element-by-element hybrid assemblage of a matrix of photosensitive elements based on MCT and a Si multiplexer with the help of In columns. For cooled IR FPAs, the problem of destruction of a hybrid assemblage can arise because of the difference in the thermal expansion coefficients of the photosensitive element and a Si multiplexer.

Correspondingly, the larger the IR FPA format, the larger the device size and the more pronounced the effects associated with a difference in thermal expansion coefficients. The use of MBE-grown MCT heterostructures on the Si substrate allows us to solve the problem of the service life of the IR FPA upon its cooling from room temperature to cryogenic temperatures.

The selection of the substrate orientation during the MBE growth of MCT is governed by a low incorporation coefficient of the Hg atoms into the crystal lattice and, as a consequence, by a high pressure of Hg vapors during the growth [Sivananthan et al., 1986]. It was established that the MCT can epitaxially grow on the (111)B surface at the lowest pressure of Hg vapors. However, the (111) plane in MCT is a twin plane, which leads to a low structural quality of the HgCdTe (111) layers because of the formation of large number of twins and stacking faults. In 1988, Koestner and Schaake [Koestner and Schaake, 1988] showed that MCT growth on the (112)B surface is possible at low Hg vapor pressures without intense twin formation, which determined this orientation as basic for the development of the growth processes of various MCT structures for IR FPAs on various substrates. However,

*Vasily. Varavin, Vladimir Vasilyev, Sergey Dvoretsky, Irina Sabinina,
Yuri. Sidorov, Aleksandr Sorochkin and Aleksandr Aseev
A.V. Rzhanov Institute of Semiconductor Physics Siberian branch of the RAS Russian Federation

the (112) orientation is sensitive to insignificant variations in the growth conditions, which determines a narrow range of optimal values for the growth of MCT with a minimal defect density [Ryu et al., 2004]. Nevertheless, intense studies and development of equipment are being carried out for MBE growth of the MCT heterostructures on large in diameter Si (112) substrates. It is shown that such structures can be used for fabrication of high quality IR FPAs in a spectral range right up to 10 μm [Carmody et al., 2008].

We studied the MBE growth of MCT heterostructures on GaAs substrates [Yakushev et al., 2009]. It was shown that the empirically determined substrate orientation (310) provides growth of high quality MCT films without stacking faults and twin lamellae also at low Hg pressures, but considerably broadens the range of optimal growth conditions.

In this study, we examined the growth of MCT heterostructures on Si (310) substrates with a diameter as large as 100 mm for IR FPAs of the spectral range of 3–5 μm and the formation and characteristics of p–n junctions and photoelectric parameters of IR photodetectors with different formats.

2. Growth process of HgCdTe/Si(310) heterostructures

HgCdTe/Si(310) heterostructures were grown using the multichamber ultrahigh vacuum MBE installation "Ob'" [Sidorov et al., 2000]. For in situ monitoring of preepitaxial preparation and growth, we used reflection high-energy electron diffraction (RHEED) and single-wave ellipsometry at wavelength λ = 632.8 nm. P-Si:B (with resistivity of 10 Ω cm) wafers 76 and 100 mm in diameter oriented along the (310) plane were used as substrates.

Before charging into a vacuum system, Si substrates were treated by the standard RCA procedure [Kern and Puotinen, 1970]. As a result, the surface was passivated with a thin SiO_2 layer. At the last stage of chemical treatment, the substrates were immersed into a 1% aqueous HF solution to remove SiO_2 and hydrogenate the surface [Fenner et al., 1989]. The substrates were charged into the installation from a sealed box in atmosphere of dry nitrogen.

Preepitaxial vacuum annealing was performed in two stages. Preliminary annealing was carried out to remove physically adsorbed contaminants. Then the sample was heated to 550–600°C in the arsenic flow. After exposure to the As_4 vapors for 15 min and cooling, the Si substrate was transported to the growth chamber of the buffer layers.

The lattice mismatch between the Si substrate and MCT is ~19%. It is eliminated by the introduction of ZnTe and CdTe buffer layers. A ZnTe layer 0.01 μm thick was grown on Si at 200–240°C. The beam equivalent pressure (BEP) for Zn was higher than the BEP for Te_2 by a factor of 20–40. A CdTe layer 6–8 μm thick was grown on ZnTe/Si at 280–320°C. The BEP for Cd was higher than the BEP for Te_2 by a factor of 3–5. MCT layers were grown on the obtained "alternative" CdTe/ZnTe/Si(310) substrate by the process described in detail in [Sidorov et al., 2000].

A specially constructed chamber was used to obtain MCT MBE heterostuctures. Usually, a substrate is rotated to obtain a uniform composition. In this case, flux densities are averaged over the area. This effect allows to obtain required uniformity. Unfortunately, it is very difficult to use precision ellipsometric methods for composition controlling while the substrate is being rotated.

To uniform the density of molecular flows over the area of the substrate the coaxial arrangement of the molecular sources is realized [Blinov et al., 1997a, 1997b]. Molecular sources with circular lenses were developed. These sources provide highly uniform

molecular flows over a large area with a minimum expense of evaporated material. The calculation shows that the homogeneity of the composition should not exceed 0.0002 cm^{-1} in the exact alignment of sources which is an order of magnitude above the most stringent requirements for uniformity. High homogeneity of flows allows to exclude rotation of the substrate and carry out continuous monitoring of the growth process.
As a result, obtained MCT MBE have high uniformity of distribution of composition over the area. For the layers with x = 0.3–0.35, the maximal variation in composition x over the surface of a sample 76.2 mm in diameter does not exceed 0.002. Such variation corresponds to the deviation of a wavelength cut-off of photosensitivity at 77 K by less than 0.1 μm (Fig. 2), which provides a high uniformity of parameters of large-size FPAs.

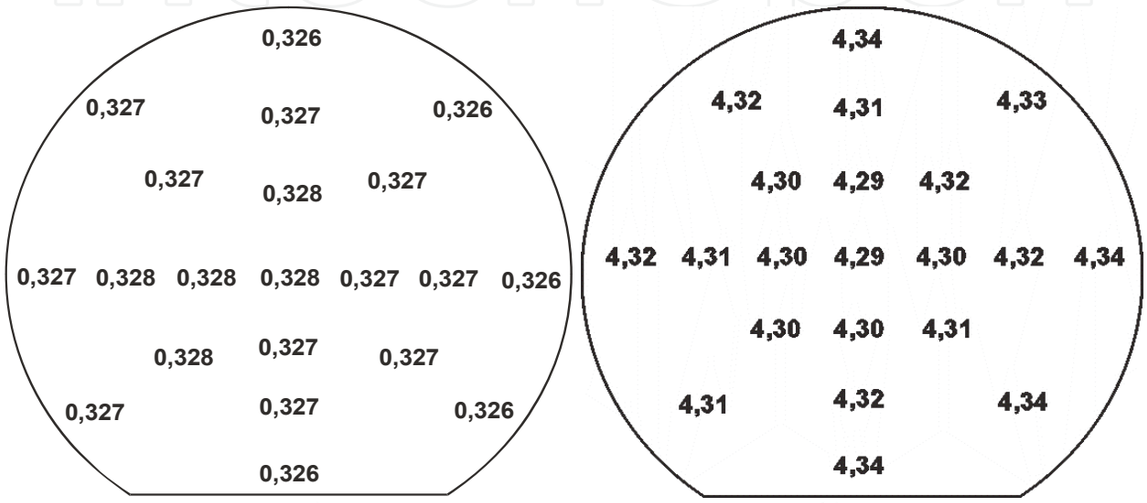

Fig. 1. Distribution of composition (a) and distribution of wavelength cut-off (microns) at 77K (b) over the area of HgCdTe/Si(310).

Due to the continuous monitoring of the growth process by *in situ* ellipsometry, MCT layers can be given composition profile throughout the thickness, such as the working layer of constant composition and graded-gap layers. Figure 2 illustrates the change in composition throughout the thickness of a typical MBE MCT heterostructure with graded-gap layers measured by the *in situ* ellipsometry. When the composition of the working layer X_{CdTe} = 0.22 the boundaries of this layer are graded-gap layers in which the CdTe content rises to the surface and to the boundary with the buffer layer. Graded-gap layers with high content of CdTe can be used for surface passivation [Bhan et al., 1996]. Increasing the width of the bandgap at the heterointerfaces and at the film surface creates built-in fields. These fields brush aside the non-equilibrium carriers from the surface which has a high rate of recombination. There is reason to believe that in this way the effective lifetime of nonequilibrium carriers can be increased [Remesnik et al., 1994;Buldygin et al., 1996;Voitsekhovsky et al., 1996].

3. Structural defects in HgCdTe/Si(310) heterostrucutures

There are three types of defects in MCT layers grown on silicon substrates: threading dislocations, stacking faults and antiphase domains. In addition, macroscopic V-defects may

exist. V-defects are complex entities that contain the area of broken structures, twin lamellae and stacking faults (SF).

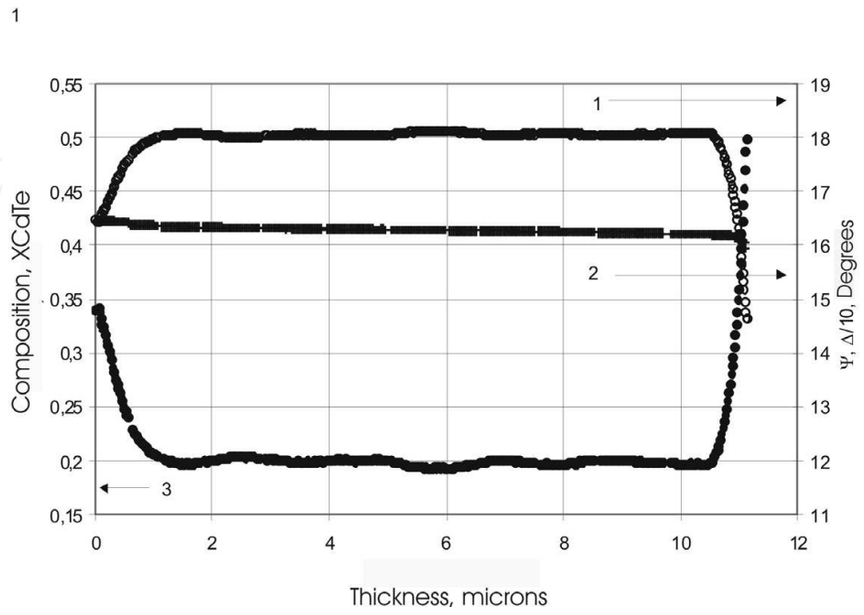

Fig. 2. Results of in situ ellipsometric measurements: 1 and 2- ellipsometric angles ψ and Δ respectively; 3- composition profile.

Studies of defects in the bulk of the films were carried out by transmission electron microscopy (TEM) and selective etching. TEM analysis was performed using the electron microscope JEM-4000EX (JEOL). Samples for TEM were prepared in the form of thin foils parallel to the growth surface, and in the form of cross sections.

To obtain transparent to the electron beam thin foils in a plane parallel to the surface of the film an original technique was developed. A sample (HgCdTe/CdTe/ZnTe/Si heterostructure) was placed in a hot KOH solution and held until complete dissolution of the silicon substrate. Then the film (HgCdTe/CdTe/ZnTe) was washed and made thinner by etching from the growth surface or from the opposite side in a solution of bromine (1.5%) in methanol. Using this method of separation of film from the substrate it is possible to investigate the structure of the film close to the surface and near the heterojunction.

Following solutions were used for selective etching: 10ml HNO_3 + 20 ml H_2O + 4g $K_2Cr_2O_7$ + 1,5 mg $AgNO_3$ (etchant E-Ag1) [Sidorov et al., 2000] and 5g CrO_3 + 3 ml HCl + 15 ml H_2O (etchant Schaake) [Kern and Puotinen, 1970]. Etchant E-Ag1 was used to detect defects in CdTe layers, and Schaake etchant for detecting defects in CdHgTe layers. As a result of selective etching, etch pits appeared on the surface. Etch pits had a characteristic shape, different for different types of defects. Dislocations were revealed in the form of elongated triangles for CdTe and in the form of points for HgCdTe. Antiphase boundaries were identified as lines of arbitrary shape, and stacking faults in the form of parallel straight lines. The density of surface macroscopic defects was measured using an optical microscope with a built-in CCD camera combined with a personal computer. This hardware and software system can automatically scan the entire surface of the heterostructure and determine the lateral distribution of defect density and defect size over the sample area.

3.1 Antiphase domains

Antiphase domains (APD) are characteristic defects for any heterostructure where the substrate is a semiconductor with a diamond lattice (Si, Ge) and the grown layer is a binary compound with the crystal lattice of sphalerite (GaAs, CdTe). The most detailed mechanism of the formation of antiphase domains and methods of obtaining of single-domain layers are considered for the case of heteroepitaxy of GaAs/Si and GaAs/Ge [Fenner et al., 1989]. The appearance of antiphase domains in GaAs layers grown on Si substrates is due to the monatomic of silicon surface. If the silicon surface contains steps of monatomic height and deposition on the terraces begins, for example, with arsenic then the second monolayer of gallium will be a continuation of the arsenic monolayer on the overlying terraces (Fig. 3a). This situation corresponds to the formation of antiphase boundaries which will lead to antiphase domains. Thus, it is necessary that the surface of the sample had steps of a diatomic height to lack of antiphase domains. Since arsenic in a wide range of conditions is adsorbed on the surface of silicon in an amount equal to one monolayer [[Blinov et al., 1997a]], the presence of diatomic steps is necessary and sufficient requirement for GaAs/Si heterostructures without APD.

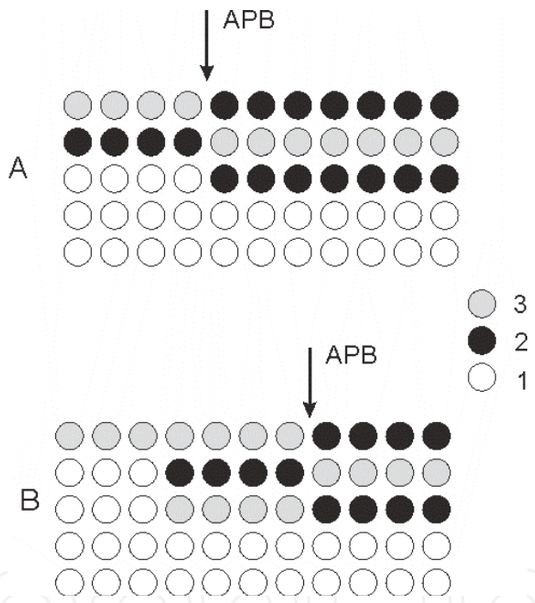

Fig. 3. Formation mechanism of antiphase boundaries. A – in case of monoatomic steps on a surface. B – in case of discontinuous absorption layer. 1 – substrate atoms, 2 – V or VI group atoms, 3 – II or III group atoms.

In case of ZnTe/Si heterostructures, the presence of diatomic steps on the silicon surface is not enough to grow films without APD. Modern technologies for high-quality structures HgCdTe/CdTe/Si require a preepitaxial annealing of the substrate in As_4 vapours [Blinov et al., 1997b; Bhan et al., 1996; Remesnik et al., 1994]. Clean Si surface is actively cooperating with the residual atmosphere of the vacuum system, in particular with tellurium [Buldygin et al., 1996], forming the centers which act as nuclei for defects of crystal structure. Adsorption of As passivates the surface of Si since excessive (relative to the silicon) valence electrons of As are completely saturating surface bonds of Si [Voitsekhovsky et al., 1996]. As a result, the amount of residual contamination on the surface of the substrate decreases

which leads to an increase in crystalline perfection of the heteroepitaxial layers. It was shown for ZnSe on Si (100) [Kuleshov et al., 1985] that the arsenic monolayer prevents the formation of amorphous layer $SiSe_x$ and significantly reduces the density of twin lamellae and stacking faults in the layers of ZnSe. It was established experimentally that the absence of As in CdTe/Si (211) heterojunction leads to polycrystalline growth [Buldygin et al., 1996].
Neither Zn nor Te is absorbed in the form of a continuous layer on the surface of As/Si (310) or clean Si (310) [Wang et al., 1976]. Tellurium is adsorbed in the form of separate islands. Zinc in the absence of Te vapors has an infinitesimal rate of insertion which begins to approach 1 only if the vapor phase contains tellurium atoms. In such circumstances, there is the possibility of the simultaneous presence on the terrace of nuclei, the lower layer of which is formed from the atoms of zinc and tellurium. This effect will inevitably lead to the formation of APB even if the terraces on the surface of the substrate are separated by diatomic steps (Fig. 1b).
It is evident from the above arguments that the formation of antiphase domains in HgCdTe/CdTe/ZnTe/Si (310) is determined not only by the structure of the substrate surface but also by the conditions of formation of the ZnTe/Si (310) heterojunction.
Using scanning tunneling microscopy and high and low energiy electron diffraction methods, the influence of vacuum annealing on the morphology of surfaces of hydrogenated Si (310) was investigated.
In a wide temperature range (500 - 1250^{0}C) surface of Si (310) has strong relief, roughness of which according to the STM was 0.15 - 0.3 nm (Fig. 4).
Nevertheless, according to the LEED there are equidistant steps of diatomic height on such a surface. The same diffraction patterns were observed by LEED for each of our samples after annealing at temperature range from 500^{0}C to 1250^{0}C. Qualitative changes of the diffraction patterns did not occur with increasing annealing temperature. Annealing at 1250^{0}C led to an increase in the brightness of reflections. An example of a diffraction pattern from the Si(310) is shown in Figure 5. Rows of reflections along the [-130] can be seen. The distance between the rows of reflections indicated by letter **a**. It can be seen that certain reflexes are split in two ones. The distance between the paired reflections is denoted as **b**. Such diffraction patterns are characteristic for a system of equidistant steps. There are two things confirming presence of steps. Firstly, the splitting reflections, and secondly, the characteristic "transfusion" of paired reflections when the primary beam energy is being varied [Kuleshov et al., 1985]. The ratio **a / b** within the measurement error is the ratio of sides of the unit cell of a smooth surface of the Si (310) (**a / b** = 1.63). The distance between the paired reflections corresponds to the larger side of the unit cell of Si (310). Based on this we can conclude that such diffraction patterns obtained from the stepped surface of Si (310) with the distance between steps equals to the size of the larger side of the unit cell of this surface. Using simple geometric calculations, we can see that in this case the step height is equal to two interplanar distances for the Si (100).
It was also found that it is necessary to achieve low concentration of residual contaminants on the surface for increasing the percentage of surface formed by diatomic steps and, accordingly, reducing the probability of formation of antiphase domains. Thus, when the concentration of oxygen and carbon on the surface is more than 5% of a monolayer (according to Auger spectroscopy), there are basically monatomic steps on Si (310). This circumstance imposes very high demands on the procedure of preepitaxial preparation and loading the substrate into the vacuum system.

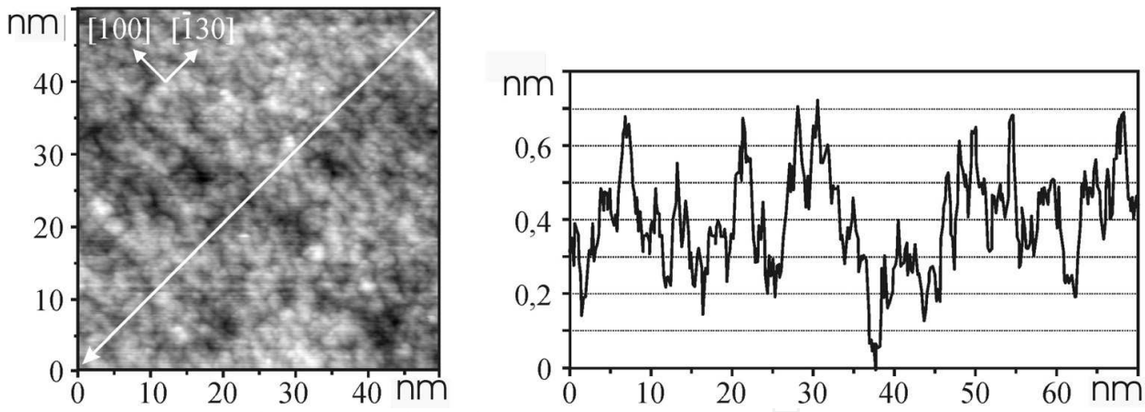

Fig. 4. STM-image of Si(310) surface after annealing at 850^{0}C.

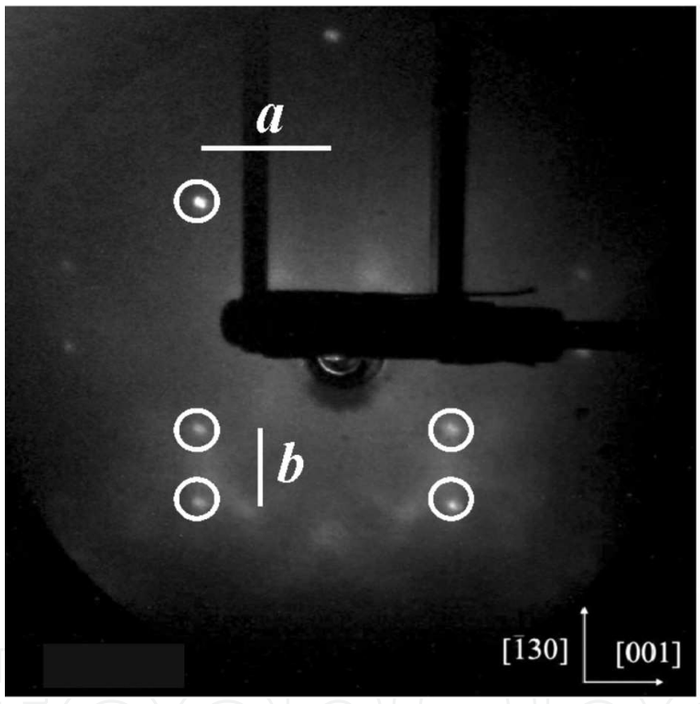

Fig. 5. Diffraction pattern of Si(310) surface after a desorption of a passivation layer at 800^{0}C. *a* - the distance between the rows of reflections; *b* – the distance between the paired reflections.

However, despite the presence of diatomic steps on Si(310), antiphase domains could occur in HgCdTe/CdTe/ZnTe/Si(310). Figure 6 shows TEM - images of CdTe surface containing the domains obtained in the pole (100). Pictures of microdiffraction received from adjacent domains are identical indicating that there is no rotation of crystal lattices in the relevant fields. As can be seen in Fig.4c, mutually perpendicular stripes with a period of approximately 18 nm elongated along [110] are observed at high magnification in the adjacent domains. Spot contrast observed along the stripes might arise due to decorating of the most active sites of CdTe growth surface. The nature of the selected linear irregularities as well as the nature of the decorating particles will not be discussed in this paper. Analysis

of images at the poles (301) and (100) allows to say that the direction of leased lines coincides with the traces of intersection of (110)-planes with the surface of the film. Since the surface of CdTe in the MBE growth conditions are usually terminated by one sort of atoms, the fact that leased lines in the domains are mutually perpendicular (at observation at the pole (100)) means that the domains are antiphase domains.

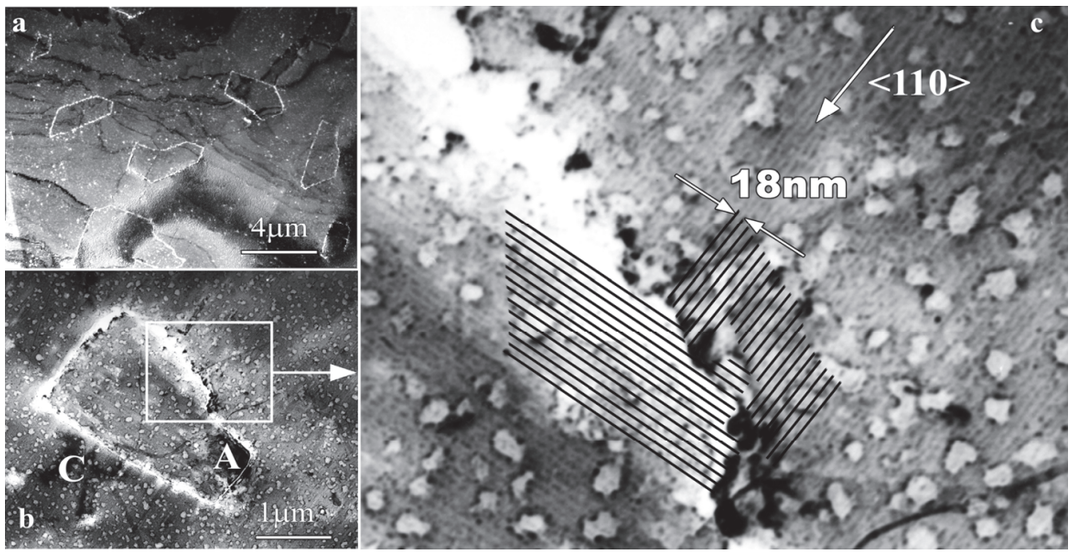

Fig. 6. TEM-images of the subsurface area of CdTe/ZnTe/Si(310) heterostucture with antiphase domains obtained in (100) pole (a), (b); (c) – boundary between two domains.

It can also be seen on Fig.6c that the antiphase boundary (APB) is a layer with structural damage. This allows us to identify the antiphase domains by chemical etching in a selective etchant followed by observation under an optical microscope.

CdTe/ZnTe/Si(310) heterostructures with CdTe thickness of 6 - 8 μm and ZnTe thickness of 0.01 - 0.02 μm were grown for establishing the connection between growth conditions of ZnTe/Si(310) and the density of APB. Only the growth conditions of ZnTe were varied, CdTe growth conditions and preepitaxial preparation processes were the same. The grown structures were etched using E-Ag1 etchant.

Comparing the growth conditions of ZnTe with the results of selective etching it was found that there are optimum conditions for the formation of ZnTe/Si(310) heterointerface without antiphase boundaries (see Figure 7a). Such conditions were the following. The substrate temperature was 200 - 220^0C with the flux of Te_2 molecules equivalent to pressure (5 - 20) • 10^{-8} Torr and the flux of Zn atoms equivalent to pressure (1 - 10) • 10^{-6} Torr. Deviation from these conditions namely a decrease of Zn flux or an increase of substrate temperature leads to the appearance of antiphase boundaries. Figure 7 shows pictures of the surface of CdTe/ZnTe/Si(310) after selective etching. Samples presented in Figure 7 were obtained under identical conditions except for growth temperature of ZnTe, which amounted to 200, 240, and 280^0C (Figures 7a, 7b and 7c, respectively). It is evident from the presented figures that the heightened over optimal temperature of growth of ZnTe leads to the heightened density of APB. A similar sequence pattern was observed in the case when the growth temperature and vapor pressure of tellurium molecules remain unchanged but vapor pressure of zinc atoms reduced. Increasing the flux of Zn atoms above the optimum does not cause the formation of APB.

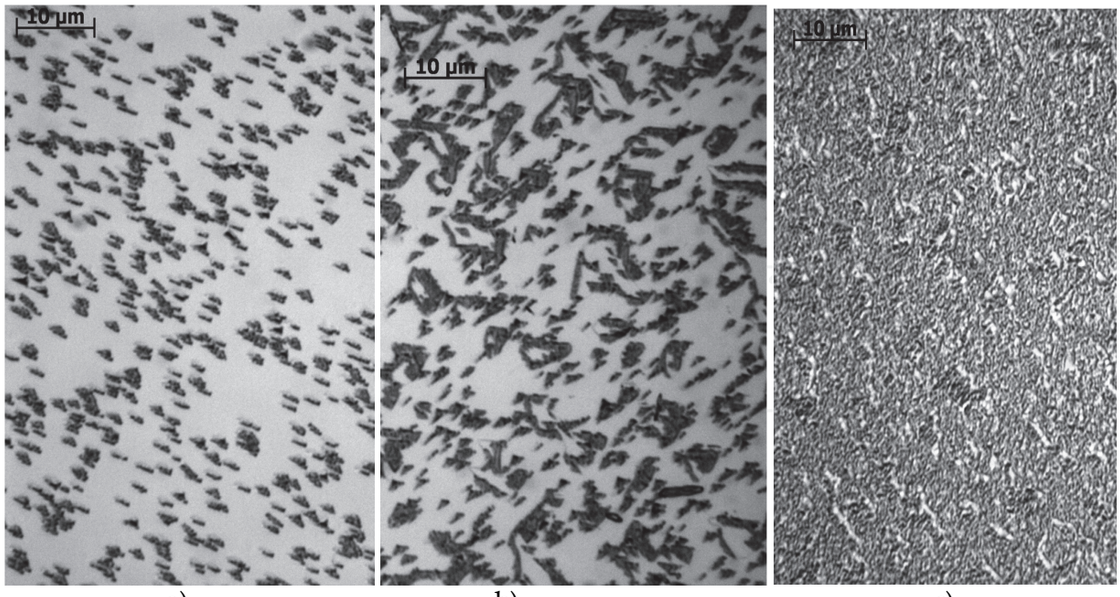

a) b) c)

Fig. 7. Etch pits on the surface of CdTe/ZnTe/Si(310) heterostructures grown at different substrate temperatures: 200^0C(a), 240^0C(b), 280^0C(c).

Growth temperature of ZnTe is 300^0C and fluxes of both components have the equivalent pressure of 10^{-6} Torr. As can be seen the optimal conditions of growth of ZnTe/Si (310) heterojunction differ substantially from optimal conditions of growth of ZnTe thick layers. The main difference is that in order to suppress the formation of APB it is necessary to decrease the temperature of the substrate and increase the vapor pressure of zinc atoms in the initial moment of growth - that is to create conditions to facilitate the adsorption of zinc. There are two types of antiphase domains for ZnTe/Si heterojunction which differ by alternating atomic layers in the heterojunction - Si-As-Zn-Te and Si-As-Te-Zn. The result can be interpreted in two ways. Firstly, we can assume that the sequence of atomic layers Si-As-Zn-Te is more favorable than Si-As-Te-Zn. Secondly, we can assume that since neither Zn, nor Te is absorbed in the form of a continuous layer we can increase the probability of one of two possible atomic configurations by making a vapor pressure of one component in 1 - 2 orders of magnitude higher than a vapor pressure of the other component.
A number of heterostructures was grown under conditions where the vapor pressure of Te_2 over an order of magnitude higher than the vapor pressure of Zn to verify the second assumption. However, ZnTe layers grown under these conditions had a polycrystalline structure according to RHEED.
The obtained results confirm the conclusion of a preference for one atomic configuration over another. This is apparently due to an excess of valence electrons at the heterointerface in case of realization of the atomic configuration Si-As-Te-Zn.

3.2 Stacking faults

Our studies revealed that there are multilayer stacking faults in HgCdTe/CdTe/ ZnTe/Si(310) These defects predominantly have a subtracting type with the density of 10^5 - 10^7 cm^{-2}. (Fig. 8a). Stacking faults lie in closely spaced parallel planes (111) intersecting the plane (310) at an angle of 68.58 degrees. Stacking faults nucleate at ZnTe/Si(310) interface and grow through the entire thickness of the film to its surface (Fig. 8b).

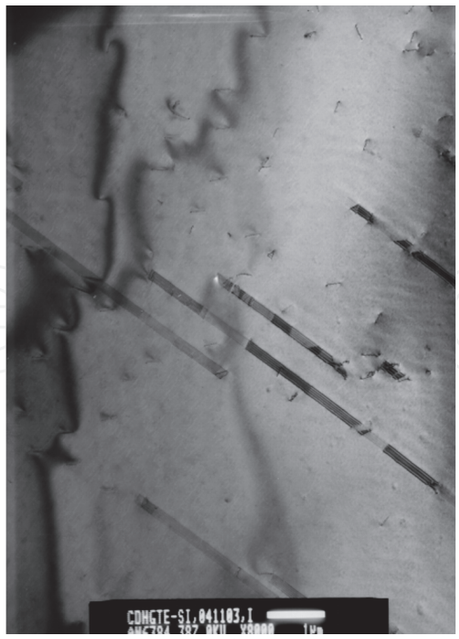

a)

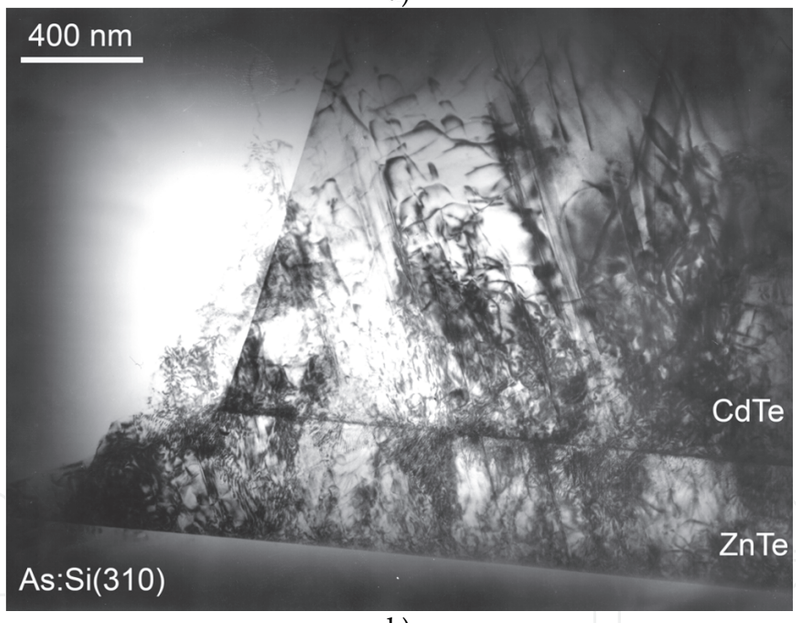

b)

a) – planar image of the subsurface area. b) – cross-section of CdTe/ZnTe/Si(310).

Fig. 8. Stacking faults in HgCdTe/CdTe/ZnTe/Si(310) heterostructure revealed by TEM.

Comparison of patterns of selective etching with TEM images of MCT film allowed to establish the relationship between the shape of etch pits and the microstructure of the film. It was established that the stacking faults revealed in the form of parallel straight lines after the selective etching (Fig. 9a). Ability to identify stacking faults by selective etching can get express information about the density, crystallography, and the distribution of stacking faults over the surface area.

In case of crystals with a sphalerite lattice stacking faults may lie in four {111} planes forming the pyramid with the (310)-plane. Intersection line of planes {111} with the (310)-plane form a quadrangle. It's diagonals lie along the [-130] and [001] (Fig.9b). Sides of this quadrangle are not parallel that allows to distinguish stacking faults occurring in each of four {111} planes. It is observed that there is an anisotropy in the distribution of stacking faults relative to the crystallographic directions [-130] and [001]. According to TEM and selective etching the density of stacking faults in the planes (111)A and (111)B differ by several orders of magnitude, and the lateral size - several times.

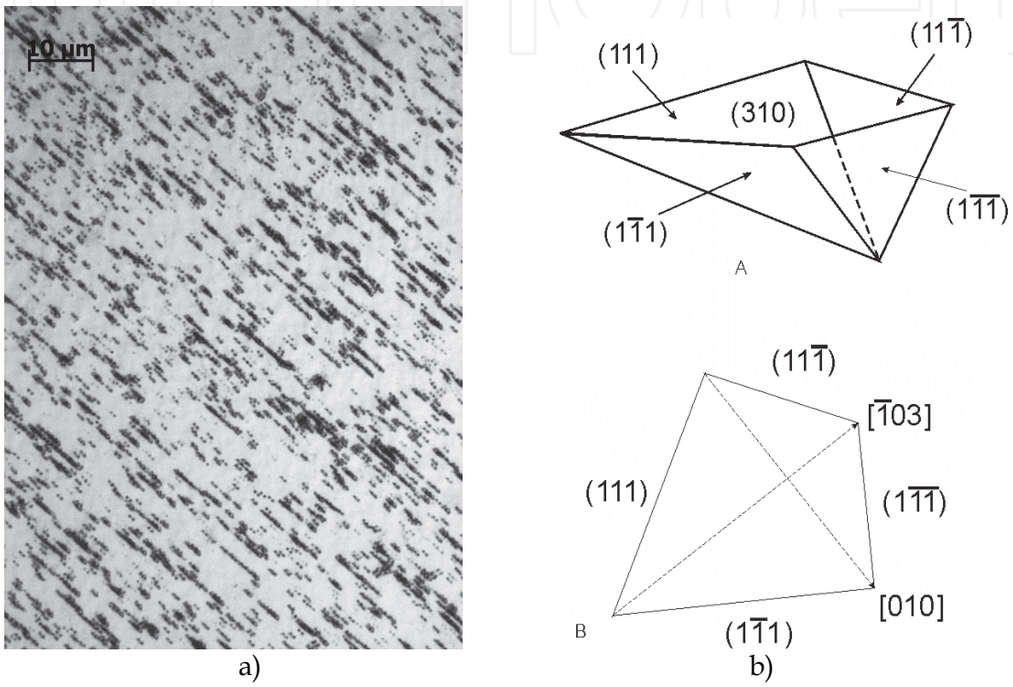

a) b)

Fig. 9. (a) - stacking faults in HgCdTe/CdTe/ZnTe/Si(310) in optical microscope after selective etching; (b) - pyramid formed by {111} planes and the quadrangle formed by the intersection of the pyramid with the (310).

There are several reasons for the formation of stacking faults in heteroepitaxy of semiconductors with a sphalerite lattice. It must be taken into account that stacking faults occur only in one of four possible {111} planes in HgCdTe/CdTe/ZnTe/Si(310). The proposed model must explain not only the formation of stacking faults but also their anisotropy. Two {111}-type planes form an angle of 43.09^0 with the (310)-plane and the other two - 68.58^0. Stacking faults lying to the boundary at a smaller angle will have a larger area than stacking faults lying at a larger angle with the same thickness of the grown layer. Accordingly, they will have a large excess energy and their formation will not be profitable. The two remaining stacking faults lie in (111) planes with different polarity. It remains to understand why one of the two different polar planes is preferable to another.

The most detailed investigation of formation of stacking faults was performed for ZnSe/GaAs(100) heterostructure. It was established that the maximum density of stacking faults observed in the case when the growth of ZnSe on substrates of GaAs (100) occurs in three-dimensional mechanism [Sidorov et al., 1996]. Stacking faults are formed on the facets

(111) that occur on the slopes of three-dimensional islands [Aoki et al., 2003]. Polarity of (111) plane in which stacking faults lie is given by the vapor pressures of Zn and Se atoms. Growth in excess of zinc leads to the appearance of stacking faults in the (111)A plane whereas growth under conditions of selenium excess causes the formation of stacking faults in the (111) plane [Sabinina et al., 2005]. Stacking faults in $A^{III}B^{V}$ layers grown on Si substrates also have the growth nature [Sidorov et al., 2001].

The lattice mismatch between film and substrate for ZnTe/Si (310) heterostructure is f = 12.3%. Therefore, the formation of stacking faults can be caused by misfit strain in a heterojunction [Rheenen et al., 2006] (formation of partial dislocations at the initial stage of stress relaxation). An indirect confirmation of this fact is, firstly, the type of stacking faults (nearly all stacking faults have subtraction type and formed by sliding of Shockley partial dislocations) and, secondly, the formation of stacking faults occurs in closely spaced parallel planes (111).

The disappearance of stacking faults after annealing may also be associated with a sliding of Shockley partial dislocations in the planes of stacking faults but the sign of these dislocations should be opposite to that of already existing Shockley dislocations. Detailed analysis of the reasons and mechanisms of the disappearance of stacking faults will be carried out in our further studies.

It is the fact for heteroepitaxy of semiconductors with a sphalerite lattice that the stacking faults lie mainly in (111) planes of the same polarity. A model was proposed in [Rogalski, 2003] to explain the anisotropy of stacking faults in ZnSe/ZnS/GaAs(001) heterostructure. According to this model the anisotropy of stacking faults is due to different slip rates of α and β dislocations. After reaching the critical thickness of the growing layer dislocation loops are formed. More mobile α-dislocation quickly reach the interface and form misfit dislocations. Less mobile β-dislocations are split into partial dislocations during the motion to heterojunction. This effect leads to the appearance of stacking faults lying in (111) planes of the same polarity. Without discussing the legality of such an approach to explain the anisotropy of stacking faults we note that in the case of ZnTe/Si(310) heterostructure the critical thickness of pseudomorphic layer is so small that the formation of misfit dislocations occurs in the first monolayer of ZnTe. In this case, the formation of partial misfit dislocations and associated stacking faults may take place. Although the stress is not fully relaxed and misfit dislocations continue to be imposed for some time of growth.

Our previous studies demonstrated that the growth of ZnTe on Si (310) occurs in three-dimensional mechanism and rate of growth is limited by the formation and growth of nuclei [Haakenaasen et al., 2002]. Therefore, in our opinion, in addition to the deformation mechanism there is also the growth mechanism of the formation of stacking faults. Such a mechanism is realized when a coalescence of three-dimensional islands occurs at the initial stage of growth just as it is described in [Aoki et al., 2003; Sidorov et al., 2001]. As it was established in this paper the formation of antiphase domains may be suppressed when the vapor pressure of Zn is more than ten times greater than the vapor pressure of Te. Creating such conditions we seem to do the preferred appearance of (111) facets of the same polarity which leads to the observed anisotropy of stacking faults.

Confirmation of the existence of the growth stacking faults in the HgCdTe/CdTe/ZnTe/Si(310) is the observed correlation between the density of stacking faults in the surface layer of HgCdTe and growth conditions of ZnTe (Fig. 10). A multilayer heterostructure with a total thickness of layers more than 10 microns was chosen as an

object of study due to the following reasons. The method of selective etching was chosen to control stacking faults because of its quickness. Also, this method allows to work with samples of a larger area as compared with the TEM method. We were unable to find a selective etchant revealing stacking faults in ZnTe and CdTe layers. The method of selective etching can be used only in HgCdTe layers. Mismatch of crystal lattices of the substrate and the heterostructure layers is very large so decreasing of a layer thickness is expressed in increasing of the density of threading dislocations until the impossibility to count the density of defects (both dislocations and stacking faults). In addition, the practical interest for production of devices based on MCT heterostructures is the defect density in the absorber layer.

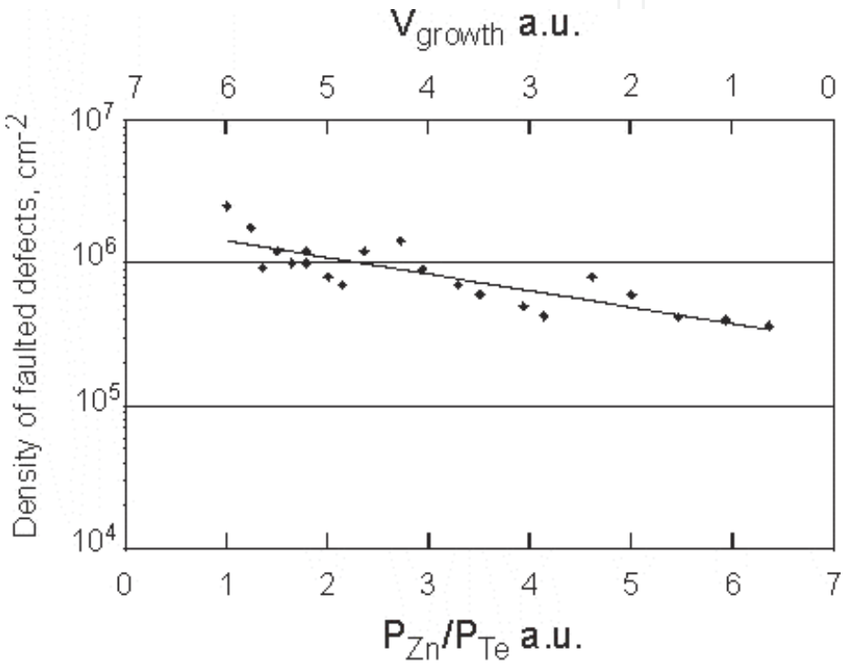

Fig. 10. The dependence of the stacking faults density on growth conditions of ZnTe for HgCdTe/CdTe/ZnTe/Si(310) heterostructures.

The source temperature of Te was varied while growing these heterostructures. Source temperatures of Zn and substrate were kept constant. Regimes of preepitaxial annealing, CdTe buffer layer growth and the growth of MCT were the same. Thickness of the ZnTe layer was in situ controlled by a single-wave ellipsometer. The growth of zinc telluride was stopped at 20 nm. The vapor pressure of Zn was constant and more than ten times greater than the vapor pressure of Te. The growth time of a layer was directly proportional to the relative of vapor pressures of Zn and Te (P_{Zn}/P_{Te}) and inversely proportional to the growth rate of ZnTe (Vgrowth). Figure 10 shows that the density of stacking faults decreases with increasing of relative vapor pressure of Zn and decreasing of growth rate. It was assumed that the growth rate affected the density of stacking faults. As it was mentioned, our previous study showed that the growth rate of ZnTe on Si (310) is limited by the formation and growth of nuclei. A lower rate of growth expresses in a lower density of nuclei (as evidenced by in situ ellipsometric measurements [Vilela et al., 2005]) and correspondingly lower density of nucleation centers of stacking faults.

Our studies have shown that annealing of HgCdTe/CdTe/ZnTe/Si(310) heterostructures in an inert atmosphere at a temperature of 200^0C - 250^0C for 5 - 10 hours leads to the disappearance of stacking faults in the whole volume of HgCdTe layer. We performed a series of annealings for a more complete understanding of the mechanism of the disappearance of stacking faults. CdTe/ZnTe/Si (310) heterostructures with thicknesses of 6 - 8 μm were annealed in different environments and at different temperatures. Annealings were performed in atmospheres of tellurium, cadmium, and in an inert atmosphere. It was found that annealing in tellurium atmosphere at 350^0C leads to the disappearance of stacking faults in the layers of CdTe (according to TEM stacking faults were absent in the entire volume of the heterostructure). Annealing in atmosphere of cadmium and in an inert atmosphere did not lead to reduction of density of stacking faults in CdTe/ZnTe/Si(310) heterostructures.

3.3. Threading dislocations

Crystal structure defects and, especially, misfit dislocations are necessary equilibrium elements of heteroepitaxial structures which provide the stress relaxation. Therefore, avoiding the generation of dislocations during heteroepitaxy is impossible in most cases and sometimes impractical because it can lead to a strong macrodeformation of an epitaxial layer until its destruction. In this regard, one of the important problems of heteroepitaxy is not the elimination of structural defects in general but the creation of optimum distribution by volume of the heterostructure. First of all, we mean the maximum reduction in the number of structural defects in the working area. These defects are the worst thing for electrical and optical properties of the material [Wang and Farlane, 1976].

Density of threading dislocations (N_{DS}) in the epitaxial film decreases from the interface to the surface. This phenomenon can be described by the equation:

$$\frac{dN_{DS}(x)}{dx} = -aN_{DS}(x) - bN_{DS}^2(x) \tag{1}$$

where x - coordinate along an axis oriented normal to the surface. The interface corresponds to x = 0, and the surface x = h, a and b-constants [Tashikawa and Yamaguchi, 1990].

Dislocations can interact with point defects, locally strained areas, other dislocations during the growth. As a result, they can change directions of propagation and reach a border of the structure. This mechanism corresponds to the first term on the right side of equation (1). The second term corresponds to the reaction between pairs of dislocations with identical Burgers vectors when approaching them to distance of interaction L^0. As a result of the reaction dislocation loops are formed and their subsequent intergrowth in the epitaxial layer becomes impossible (the constant b is proportional to L^0).

The solution of equation (1) has the form:

$$N_{DS}(x) = [\left(N_{DS}(0)^{-1} + b/a\right)exp(ax) - b/a]^{-1} \tag{2}$$

The interaction of dislocations is the dominant process at small thicknesses (h <50 μm) typical for the MBE and the solution (1) takes the form:

$$N_{DS}(x) = \left[N_{DS}(0)^{-1} + bx\right]^{-1} \tag{3}$$

Effect of $N_{DS}(0)$ on the value of $N_{DS}(x)$ is relatively small especially when h> 1 μm. The parameter b is determined by the growth conditions. If growth conditions are standard then the curves NDS (x) for various systems are sufficiently close to one another. This is confirmed experimentally in [Sheldon et al., 1988] for InAs / GaAs, GaAs / Ge / Si, GaAs / InP heterostructures grown by MOCVD. In this case, NDS (x) ~ 10^9/x at h> 0.5 microns (here the dimension of the N_{DS} (x) – cm^{-2}, x – thickness in microns).
Molecular-beam epitaxy, as a rule, provides the N_{DS} values in surface regions of films at 10^8-10^6 cm^{-2} at h> 5 microns.
At the present time the method of selective etching is used to identify the threading dislocations. The density of etch pits is used as a parameter of structural quality in most studies of photodiodes on the basis of MCT. Figure 11 shows the density distribution of etch pits in layers of CdTe grown on Si (310).
Dependence of the density of etch pits on the layer thickness is satisfactorily described by the expression (3), b = (7.0-9.0)*10^{-5}. That is, the final density of threading dislocations in CdTe / Si (310) heterostructures is determined by reactions between pairs of dislocations with identical Burgers vectors.

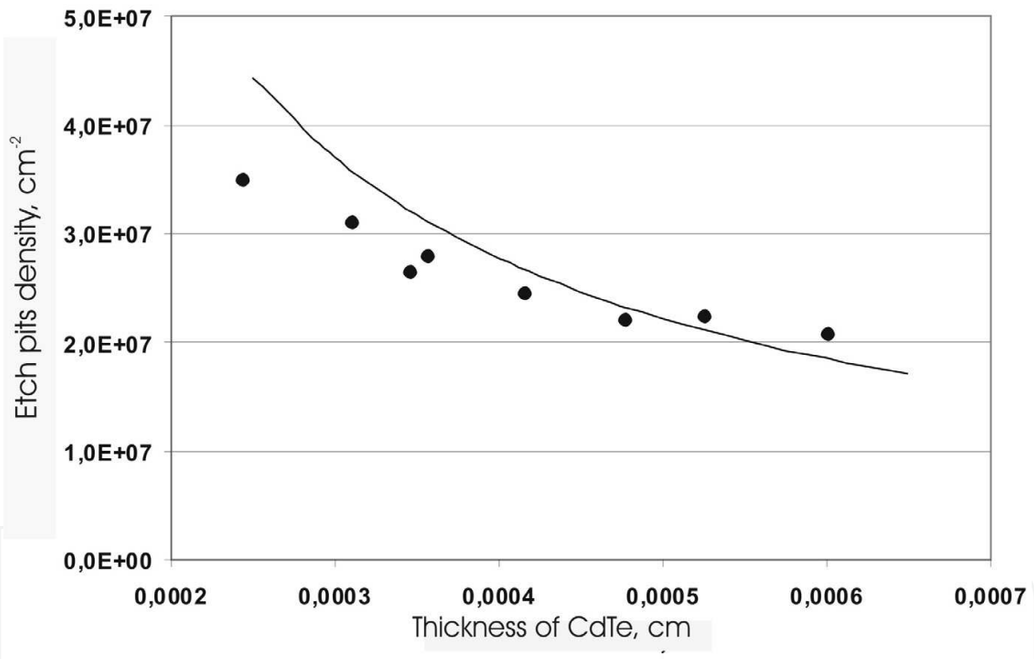

Fig. 11. Etch pits density distribution throughout the thickness of CdTe grown on Si(310). Dots – experimental results, full line – calculated results.

It can be seen from the data presented in Figure 11 that the thickness of the film CdTe h = 5 - 7 microns provides the dislocation density in the surface region $N_{DS} \approx 10^7$ cm^{-2} when grown on Si (310). Further reduction of N_{DS} without increasing the thickness of the film requires serious efforts.

3.4 V-defects

The mercury vapor pressure is less than 10^{-3} Torr at typical growth temperatures of MCT MBE (180-200^{0}C) which does not match the definition of the conditions of molecular beam

epitaxy - molecules or atoms of the deposited material must reach the substrate without collisions with other atoms or elements of the chamber construction.
Thermodynamic analysis shows that the MBE growth of HgCdTe films is carried out in conditions where two phases - $HgTe_{cr}$ and Te_{cr} - are stable [Sidorov et al., 1996]. Figure 12 shows the calculated dependence of supersaturation on the deposition temperature for HgTe (curve 1) and Te (curve 2) at a mercury pressure of 10^{-3} Torr and deposition rates 1 μm / hour. As the temperature decreases below a critical level (T_1) the crystallization of tellurium becomes possible while the crystallization of mercury telluride even impossible. With further temperature decreasing (below T_2) the formation of crystalline mercury telluride is thermodynamically possible but the possibility of deposition of elemental tellurium is also saved.

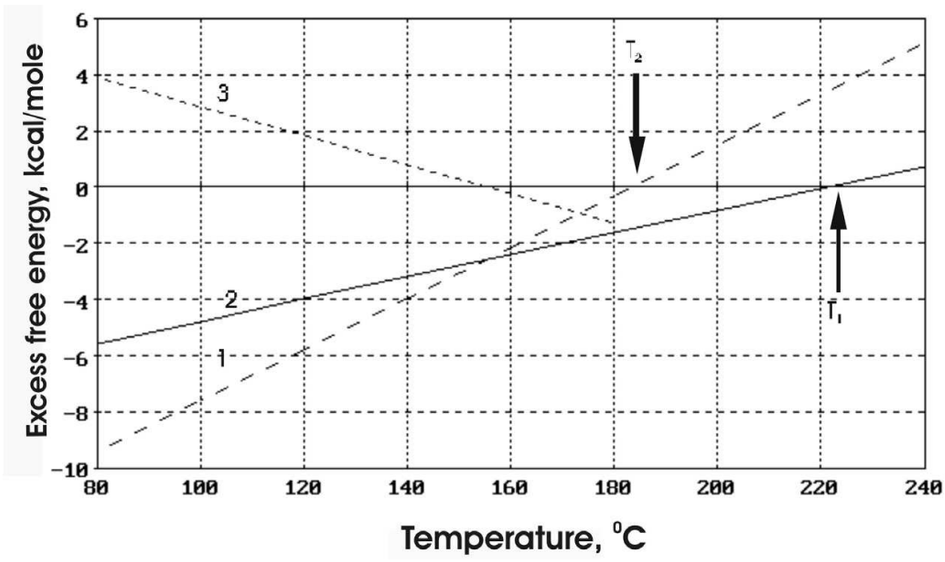

Fig. 12. Temperature dependence of superstauration. Curve 1 – for HgTe (deposition is possible at $T<T_2$). Curve 2 – for Te (deposition is possible at $T<T_1$).

The only stable phase in the temperature range $T_1> T> T_2$ is tellurium. The formation of a polycrystalline film of tellurium is observed at these temperatures by RHEED in situ. HgTe and Te phases are stable simultaneously when $T <T_2$. A predominant formation of one of the phases is determined solely by the kinetics of formation of the corresponding phases when there is a thermodynamic probability of formation of several phases. There is reason to believe that HgTe phase has a higher rate of forming. This fact is possible due to the relatively large vapor pressure of mercury and is indicated by experimental results. During the crystallization of tellurides supersaturation of tellurium is decreased. In the extreme case, when the formation of HgTe is close to equilibrium the vapor pressure of tellurium drops to a value

$$P_{Te2(eff)} = K_{dissHgTe} / P_{Hg}$$

Then the effective supersaturation of Te (Fig. 12, curve 3) decreases.
Thus, if the formation of the HgTe phase does not meet kinetic barriers, the probability of the formation of elemental tellurium phase is reduced. If, however, the crystallization of

HgTe is hampered, the probability of the formation of elementary tellurium increases. The main problem is the fact that tellurium evaporates and reaches the surface of the growing MCT film as a diatomic molecule. The process temperature is so low that tellurium which did not react with mercury and cadmium can not reevaporate.

Figure 13 schematically shows the main possible processes occurring at the surface with the participation of tellurium. Molecules of tellurium involved in two processes: the dissociation of molecules and the crystallization of a perfect MCT film and crystallization of tellurium as a separate phase when the dissociation process does not have time to occur. In the last case, the formation of tellurium phase on the surface breaks the crystal growth of MCT and leads to the avalanche multiplication of defects in the accordance with aforesaid the difficulties in crystallization of MCT in the defect sites increase the possibility of formation of elemental tellurium. As a result, formation of specific threading defects, so-called V-defects (or voids) [Aoki et al., 2003], takes place. These defects avalanchely grow to the surface. Such defects are hallmark patterns of MCT grown by MBE.

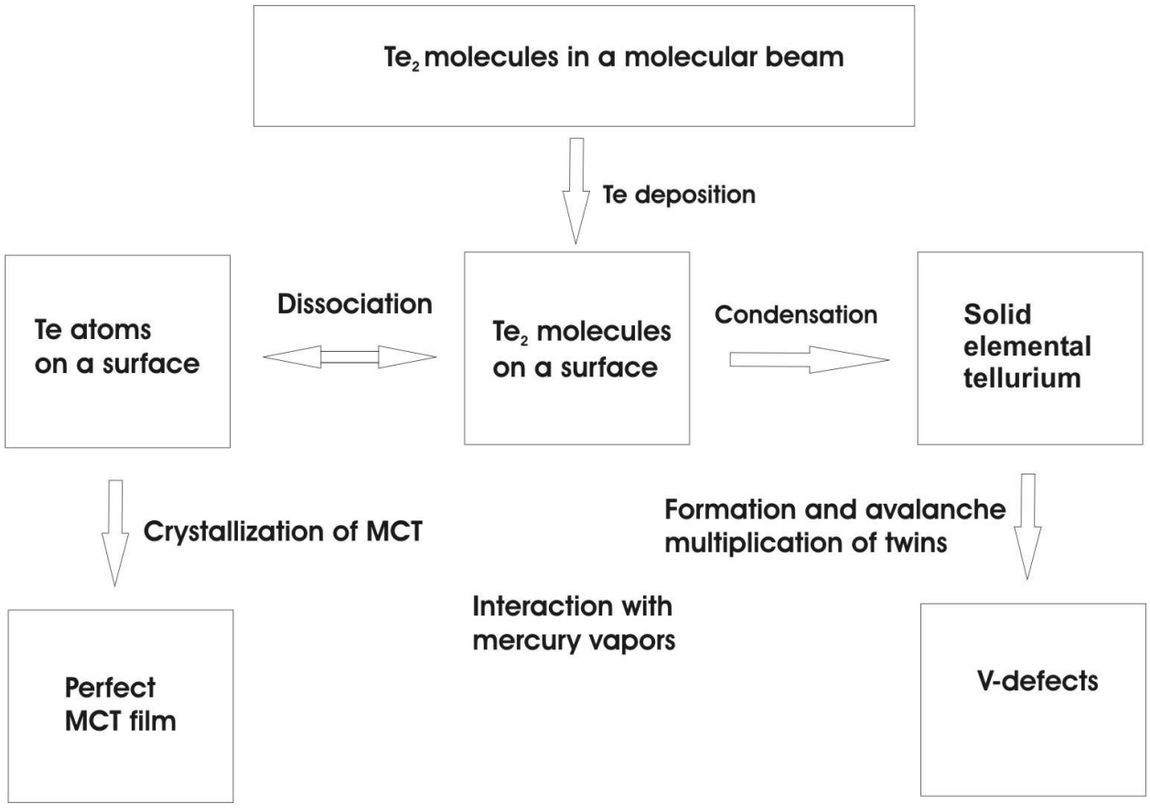

Fig. 13. Processes involving tellurium occurring at the surface during the growth of MCT.

For modern practical device applications MCT MBE with a density of V-defects ~ 10^3 cm^{-2} is used.

The process of growth of MCT film with a low density of V-defects requires precise maintenance of the growth conditions and high surface quality of the buffer layer. At non-

optimal growth conditions like lack or excess of mercury, original inhomogeneity of the substrate surface (relief or a high density of defects which can be linked together) take place there is the possibility of irreversible deterioration of surface and structure of MCT during MBE. Also one of the causes of V-defects is the perturbations of the relief [Sabinina et al., 2005].

Comparison of results of selective etching with a density of macroscopic V-defects allowed to establish a correlation between the density of V-defects and the density of antiphase domains in HgCdTe / Si (310) heterostructures.

Optimized conditions of preepitaxial preparation processes of the substrate and growth of ZnTe and CdTe buffer layers allow to obtain HgCdTe/Si(310) heterostructures without antiphase boundaries. Optimization of the growth process and the absence of antiphase boundaries have reduced the density of morphological V-defects to a value of ~ 1000 cm^{-2}. Also, these defects have the uniform distribution over the surface (Fig. 15a). Fig. 15b shows the appearance of MCT MBE 100 mm in diameter. The structure surface is the mirror-smooth and allows to create photosensitive elements by planar technology.

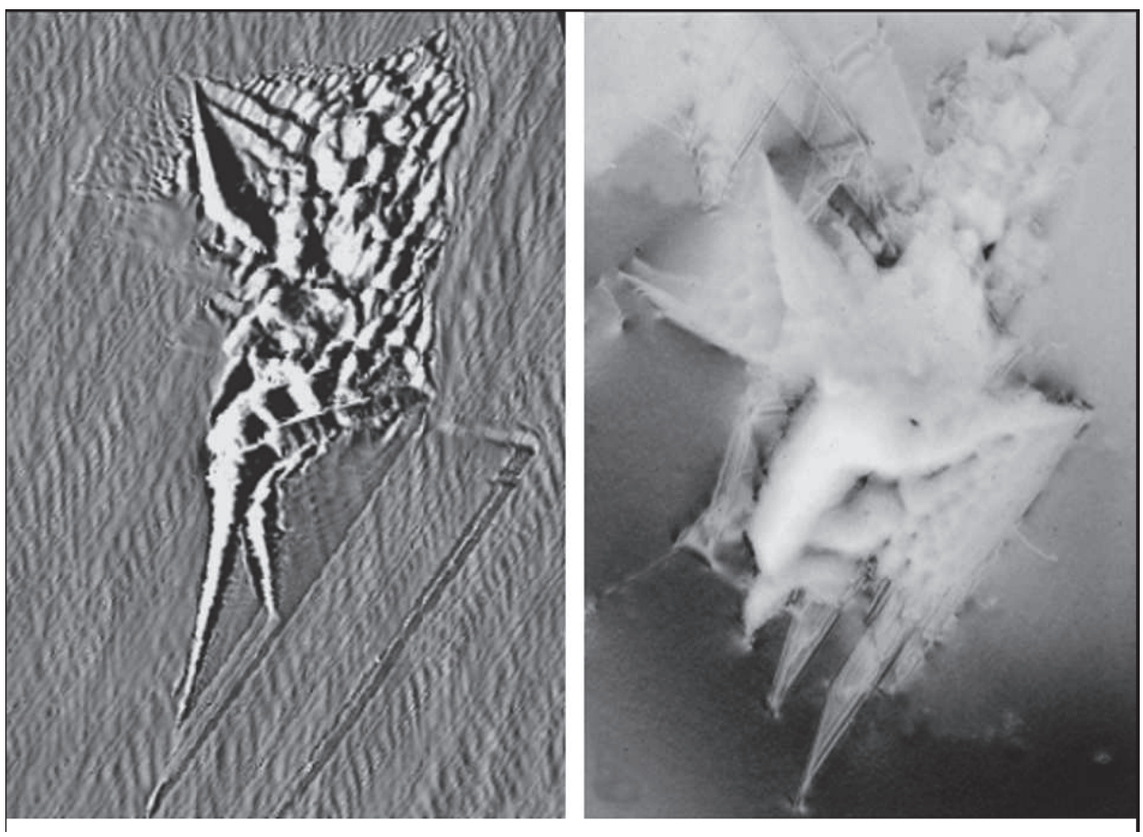

Fig. 14. Typical AFM (a) и TEM (b) 12×12 μm^2 images of a V-defect consisting of stacking faults, twin lamellae и defect structure area on the surface of HgCdTe(310).

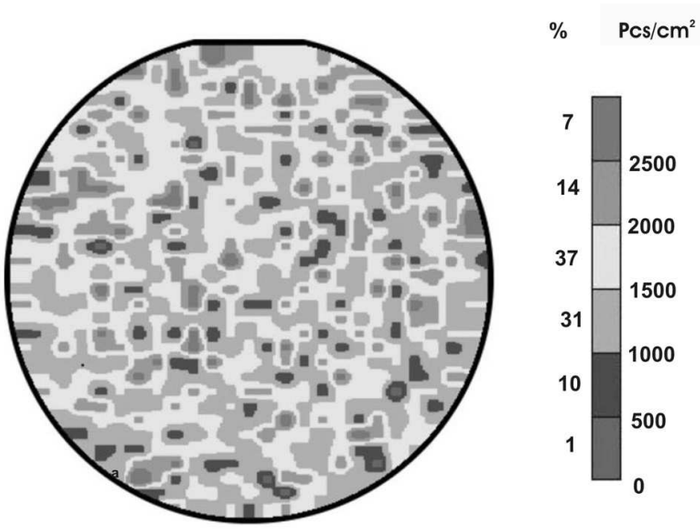

a)

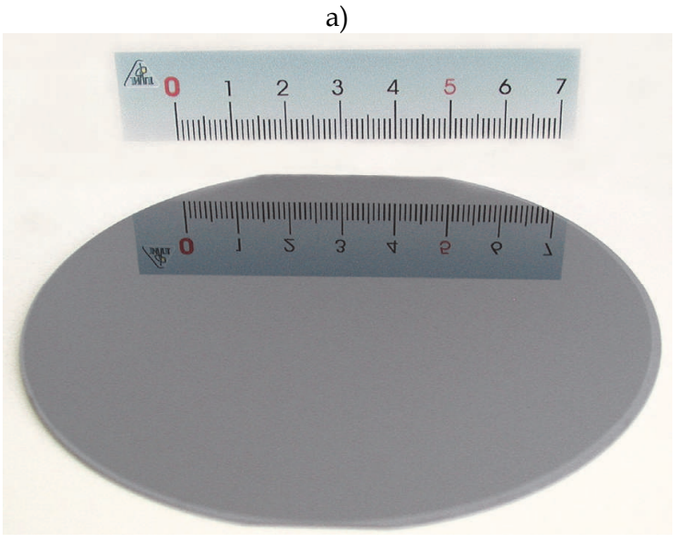

b)

Fig. 15. Distribution of V-defects over the area (a) and appearance (b) of HgCdTe/Si(310)

4. Electrophysical characteristics of HgCdTe grown on Si(310) substrates

As-grown undoped MCT films have n-type conductivity regardless of the substrate (GaAs or Si). Structures of p-type conductivity were obtained by isothermal annealing in helium atmosphere at an annealing temperature 230^{0}C, mercury temperature 30^{0}C and the duration of annealing of 20 hours. Ampoules filled with gas (hydrogen or helium) were used for the heat treatments. The dependence on the results of annealing of the type of gas were not observed. Ampoule was placed in a two-zone furnace. One zone is intended to heat a reservoir of mercury, and the second - to heat the sample. Conversion to a p-type conductivity is reversible. Annealing at 230^{0}C and more than 180^{0}C mercury temperature gives again n-type conductivity.

Carrier concentration in n-type films are in the range of 1×10^{14} cm^{-3} to 1×10^{15} cm^{-3} regardless of the composition of grown layer. Calculations of equilibrium concentrations of the donor

centers introduced as intrinsic point defects and impurities show that, in MBE, the equilibrium concentration of donor centers does not exceed the level of 10^7-10^{10} cm^{-3}. Model of nonequilibrium dissolution of defects in the MCT, taking into account a deviation from equilibrium, predicts the increase in concentration of antisite tellurium to values 10^{14}-10^{15} cm^{-3}. Experimental facts on the influence of annealing conditions on the properties of MCT films allow to suggest the presence of mobile acceptor centers with variable concentration. Donor centers can also be presented. Their concentration depends on the growth conditions. It was found that the major donor centers in the films of MCT grown by MBE, apparently, are the tellurium atoms in antisite positions [Sidorov et al., 2001].
The values of electron mobility and lifetime of photoexcited carriers in MCT layers with different compositions can vary by almost two orders of magnitude. The values of electrical parameters of HgCdTe/Si heterostructures with different composition at 77 K are shown in Table 1.

Composition X_{CdTe}	Carrier concentration cm^{-3}	Mobility $cm^2/(Vs)$	Minority lifetime
X=0.22 n-type	(1-10)×10^{14}	30000-70000	0.2-1.0 μs
X=0.22 p-type	(5-15)×10^{15}	200-400	10-20 ns
X=0.3 n-type	(1-10)×10^{14}	15000-30000	5-15 μs
X=0.3 p-type	(5-15)×10^{15}	200-300	35-50 ns

Table 1. Electrical characteristics of HgCdTe/Si at 77K

The majority mobility and minority lifetime of charge carriers in heterostructures CdxHg1-xTe/Si are somewhat lower than in the MCT layers grown on lattice-matched substrates. Especially noticeable difference is observed for the n-type conductivity.
It was established on the example of heterostructures with composition x = 0.3 that the density of stacking faults and misfit dislocations influence on the mobility of electrons in the structures. Figure 16 shows the corresponding dependences.
It is seen that the mobility depends weakly on the density of dislocations. Dependence of the carrier mobility on the density of stacking faults can be divided into three areas. When the density of stacking faults is less than 2.5 × 10^6 cm^{-2} (area 1 on the chart) it is possible to obtain values of carrier mobility close to the theoretical maximum for MCT with composition x = 0.3 (40000 $cm^2V^{-1}s^{-1}$). When the density of stacking faults is in the range from 2.5 × 10^6 cm^{-2} to 5.5 × 10^6 cm^{-2} (area 2 on the chart), the carrier mobility varies from sample to sample in a wide range and can take both high enough and low values. Apparently, the density of stacking faults still not large enough to degrade the electrical properties of structures and other factors that limit mobility have high influence. When the density of stacking faults is more than 5.5 × 10^6 cm^{-2} (area 3 on the chart), the high mobility of the carriers are not observed. We can say that such a high density of stacking faults leads to the degradation of electrical properties. At the same time, it is clear that it is possible to obtain structures with high carrier mobility close to the theoretical limit despite the presence of stacking faults.

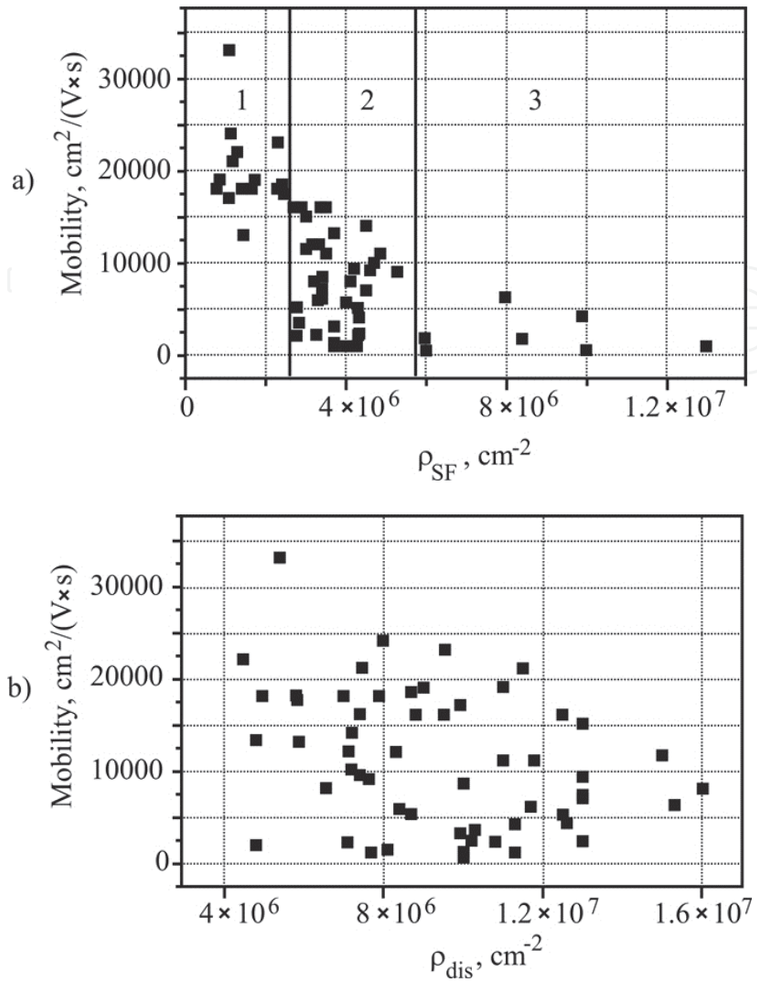

Fig. 16. Dependence of charge carrier mobility on stacking faults density (a) and misfit dislocations density (b).

5. Properties of photodiodes based on HgCdTe/Si(310) heterostuctures

5.1 Mid-wavelength spectral range

Photosensitive arrays 320 × 256 with a step of 30 μm and 640 × 512 with pixel size of 25 μm for the spectral range of 3–5 μm were fabricated from the p-type MCT structures with x = 0.29–0.33 using ion implantation of boron, and their characteristics were measured.

The current–voltage (I–V) characteristics, differential resistance, and ampere–watt sensitivity of photodiodes were measured in a nitrogen cryostat. The measurements were performed for a sample of a matrix photosensitive element with In bumps. One electric contact was constantly connected to a base layer of the photosensitive array, while the second contact was formed via lowering a mobile probe onto a selected photodiode. A photocurrent was measured under illumination from a background at 293 K from the side of In bumps through a ZnSe-based cryostat window (aperture angle θ was 36°).

Figure 14a shows the dependence of the dark current (I_d) under a bias voltage of –100 mV on the inverse temperature for a diode fabricated of the structure with a composition x = 0.328. It is seen that, in a temperature range of 160–300 K, the variation in the dark current is

proportional to n_i^2 and is determined by the diffusion mechanism [Rheenen et al., 2006]. In a temperature range of 140–160 K, I_d is proportional to n_i and is caused by generation–recombination processes in the depletion region.

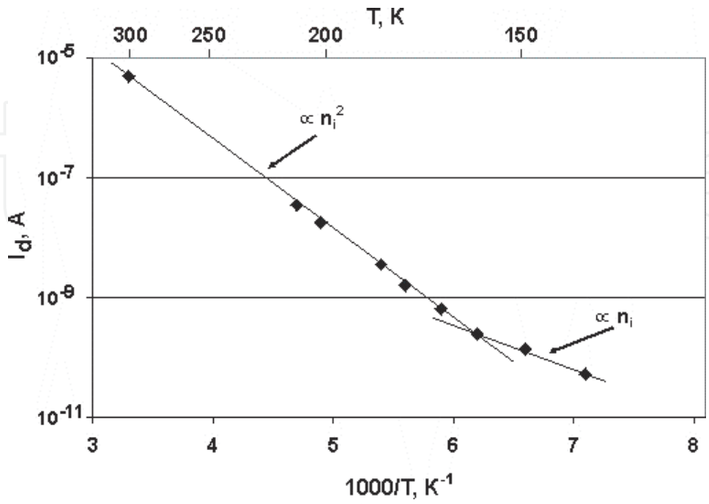

a)

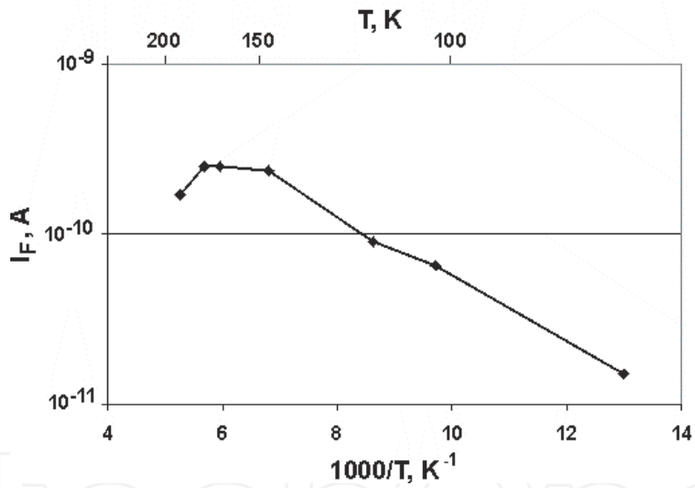

b)

Fig. 14. Dependence of the dark current (a) and photocurrent (b) on the inverse temperature at -100 mV for photodiodes based on $Hg_{1-x}Cd_xTe$ with x=0.328. Dots – experimental results. Full lines – calculated dependencies.

Photocurrent I_F (Fig. 14b) is peaked in a temperature range of 160–180 K. At temperatures lower than 160 K, the photocurrent increases as the temperature is increased, which agrees with other published data. According to [Kuleshov et al., 2005], the diffusion length of minority charge carriers in the MCT-based photodiodes with x = 0.31 continuously increased in a temperature range from 50 to 210 K due to an increase in the lifetime, while the photocurrent is proportional to the diffusion length. The peak of the photocurrent at 150–180 K can be attributed to the effect of variation in the band gap as temperature is changed which leads to a shift of the absorption edge to shorter wavelengths. As the temperature increases from 77 to 200 K, the long-wavelength photosensitivity region

decreases from 4.3 to 4 μm and the photocurrent from the background illumination decreases by a factor of 2. An increase in the diffusion length is insufficient to compensate for a decrease in the photocurrent, which leads to the emergence of a peak at 160–180 K in the temperature dependence of the photocurrent.

Comparing the plots of the dark current and photocurrent and assuming that the photocurrent increases by a factor of 2 upon illumination without shadowing with the In bump and is 0.5 nA, we can find the temperature of equality of the dark current and photocurrent, which is T ≈ 170 K. Thus, above 170 K, the background-limited mode is not realized.

To characterize the photodiodes, the product of differential resistance at a zero bias (R_0) by its optical area (A) R_0A is often used. The value of R_0 is determined directly from the measured I–V characteristics. To evaluate A, let us use the dependence of the photocurrent on the density of the photon flow and collection area of the photogenerated charge carriers [Rogalski, 2003]:

$$I_F = \eta q Q(\theta) A \tag{4}$$

where η is the quantum efficiency (the number of electron–hole pairs generated by an incident photon), q is the elementary charge, A is the collection area of the photogenerated carriers, and $Q(\theta) = Q(2\pi)\sin 2(\theta/2)$ is the density of the photon flux in the aperture angle θ from an absolutely black body with temperature T =293 K in a wavelength range from 0 to $\lambda_{1/2}$ μm, where, in turn,

$$Q(2\pi) = (2\pi c\lambda^{-4}) / \exp((hc / \lambda kT) - 1) \tag{5}$$

It was taken into account in calculations that the illumination with the background light is equivalent to the use of a black body with emissivity of 0.95, η = 0.7, and the ZnSe window used in the experiment can reflect up to 30% of the incident flux.

Taking into account the measured values of the photocurrent and using formulae (1) and (2), we can determine the collection area of photogenerated carriers A, which was in a range of 100–200 μm² for all samples. Physically, this area is a ring around the In bump (we assume that the bump itself is opaque); then, via the addition of the area of the In bump to the obtained value (we assume that the In bump is circular with a radius of 10 μm), we obtain the optical area of the p–n junction A. Multiplying A by the value of differential resistance at the zero bias R_0, we obtain the value of R_0A.

Another important parameter of both the diode itself and its material is the diffusion length of charge carriers. Assuming that the p–n junction is of circular geometry and subtracting its metallurgical radius from the optical radius of the p–n junction, we can determine the diffusion length of charge carriers. In this case, we can take into account that the geometry size of the p–n junction exceeds the size of the window for doping (a circle 10 μm in diameter) due to Hg diffusion by 2–3 μm [Haakenaasen et al., 2002].

The measured values of the photocurrent and differential resistance under the zero bias for the photodiodes fabricated from MCT of various compositions as well as the values of the diffusion length and R_0A calculated based on these parameters are listed in the Table 2.

The obtained estimated values of the diffusion lengths are smaller compared with the results of [Kuleshov et al., 1985] approximately by a factor of 2. The cause of this may be that the authors of [Kuleshov et al., 1985] grew MCT on the lattice-matched CdZnTe substrates and the density of structural defects was considerably lower than for the layers discussed in our study. A decrease in the defect density can lead to an increase in the lifetime and

mobility of photogenerated carriers and, as a consequence, to an increase in the diffusion length. Our values of R_0A do not exceed the results given in publications concerned with MCT photodiodes grown on Si substrate [Vilela et al., 2005].

Sample	X_{CdTe}	$\lambda_{1/2}$, μm	Photocurrent, A	R_o, Ohm	R_oA, Ohm·cm^2	$L_{diff.}$, μm
MCT090316	0.327	4.3	$2.0 \cdot 10^{-11}$	$4 \cdot 10^{11}$	$1.7 \cdot 10^{6}$	4.5
MCT081023	0.328	4.3	$3.5 \cdot 10^{-11}$	$3 \cdot 10^{11}$	$1.5 \cdot 10^{6}$	5.5
MCT090305	0.289	5.2	$2 \cdot 10^{-10}$	$2 \cdot 10^{11}$	$1.0 \cdot 10^{6}$	5.7
MCT090302	0.293	5.1	$1.5 \cdot 10^{-10}$	$2 \cdot 10^{11}$	$9.7 \cdot 10^{5}$	5.4

Table 2. Photoelectric properties of photodiodes based on MCT heterostructures with different composition

5.2 Long-wavelength spectral range

Photosensitive arrays 288 × 4 of standard topology [Vasiliev et al., 2004] with a detector pitch in scan of 43 μm for the spectral range of 8–12 μm were fabricated from the p-type MCT structures using ion implantation of boron, and their characteristics were measured. Pixel size is 28×25 μm.

The dark current-voltage characteristic of the real photodiode is formed as a result of the superposition of several components caused by different mechanisms. Currently, there are the following mechanisms:

- Diffusion current
- Generation-recombination current
- Tunneling current (band-to-band tunneling and trap-assisted tunneling)
- Surface currents

Diffusion current is a fundamental mechanism of charge transport in photodiodes based on p-n junctions. The total density of the diffusion current is determined by the contribution of the electron and hole currents from both sides of the junction.

Generation-recombination current can exceed the diffusion current, especially at low temperatures, although the width of the space charge region is much smaller than the diffusion length of carriers. Generation rate in the depletion region strongly depends on the applied bias voltage and may greatly exceed the rate of generation in the bulk material.

Tunneling current is caused by electrons tunneling directly through the junction from the valence band into the conduction band (direct tunneling) or through the trap levels in the junction region. The latter is a two-stage process in which the first phase is the thermal transition between one zone and a trap, and the second is the tunneling between a trap and the other zone. Tunneling process in this case occurs at lower fields compared to the direct band-to-band tunneling as electrons tunnel at a shorter distance. The tunneling current depends strongly on the band structure, the applied bias voltage, the effective dopant concentration and weekly on the temperature and the shape of the barrier in the junction.

The most controversial contribution to the formation of the dark current of a real diode is made of surface effects. Component of the dark current associated with the surface may depend not only on the type of passivation layer and method of its coating but also on the quality and composition of the MCT material.

Each component of the current depends on voltage and temperature in its own way. Many researchers suggest that only one mechanism is dominant in a particular bias range . This

method of analysis of current-voltage characteristics is not always correct. The best solution is the numerical simulation of the superposition of current components at different temperatures and bias voltages using the experimental data.
Diffusion current in n+-p junction can be described by the following equation:

$$I_{dif} = \frac{qAn_i^2}{N_a}\left[\frac{kT}{q}\frac{\mu_e}{\tau_e}\right]^{1/2} C\left(\exp\left(\frac{qV}{kT}\right)-1\right) \tag{6}$$

where A – area of the junction, N_a – acceptor concentration in lightly doped p-region, n_i – intrinsic concentration, μ_e and τ_e – electron mobility and lifetime respectively, V – bias voltage, C - factor associated with the surface recombination rate S.
Formula (6) describes the electron current from the p-type region in n-type region. If need to take into account the hole current from the n-type region in p-type region the parameters of the electrons should be replaced by the relevant parameters of the holes.
The following equation (reverse bias) was used to calculate the current component due to generation in the depleted region [Schoolar et al., 1992]:

$$I_{g-r}[V<0] = \frac{qAn_iW_{dep}V}{V_t\tau_{g-r}} \tag{7}$$

where τ_{g-r} – generation-recombiantion lifetime depending on a trap concentration N_t, $Vt=(V_{bi}-V)$ – the full potential of the junction, V_{bi} – built-in voltage of the junction, W_{dep} – width of the depletion region. In case of forward bias:

$$I_{g-r}[V>0] = \frac{2An_iW_{dep}kT}{V_t\tau_{g-r}}\sinh\left(\frac{qV}{2kT}\right) \tag{8}$$

Another component of the dark current is tunneling through the traps. According to [Gopal et al., 2001]:

$$I_{tat} = qAN_tW_{dep}W_cN_c \tag{9}$$

where N_t – trap concentration, W_cN_c – tunneling probability.
Current of band-to-band tunneling can be described by the following equation [Gopal et al., 2001]:

$$I_{btb} = \frac{\sqrt{2m_e}q^3E(V-V_{bi})A}{4\pi^3\left(\frac{h}{2\pi}\right)^2\sqrt{E_g}}\exp\left(-\frac{\pi\sqrt{m_eE_g^3}}{2\sqrt{2}qE\frac{h}{2\pi}}\right) \tag{10}$$

where m_e – electron effective mass, h - Planck's constant, E – electric field in depletion region.
Boron is not electrically active impurity in our p-n junction. Ion implantation with boron causes the area of mercury enrichment at the surface of p-type MCT due to radiation defects. Mercury diffuses from this region into the bulk and restores the original n-type conductivity at a certain depth filling the vacancies in the metal. Based on this mechanism of the formation of p-n junction, measured characteristics of MCT layers were used for calculating

the parameters of the photodiode. Characteristics are listed in Table 1. The thickness of the n-layer was taken equal to 2 microns. Due to the lack of detailed information on the energy of traps in the material we consider a single Shockley-Read-Hall level in the mid of bandgap which is quite widely used method [Rogalski, 2003]. Capture cross sections of electrons and holes are assumed to be $\sigma_n = 10^{-16}$ cm^2 and $\sigma_p = 10^{-17}$ cm^2 respectively.
Experimental and calculated current-voltage characteristics for diodes fabricated from MCT with x = 0.231 (λc = 9.06 μm) are presented in Fig. 15.

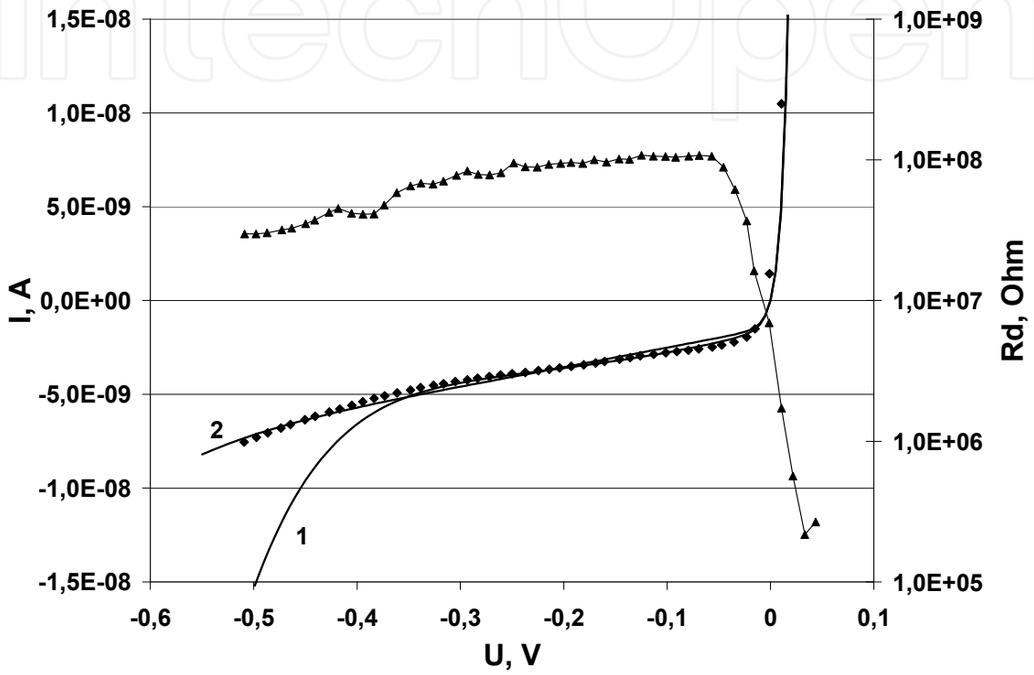

Fig. 15. Current-voltage and differential resistance-voltage characterisitics for a typical diode with λ_c=9.06 μm. Dots - experimental results; full lines – calculations.

Diffusion current is a fundamental value that does not depend on the applied reverse bias. Contribution of the diffusion current in the dark current is negligible and is about 10^{-11} A for given parameters of the MCT material. The band-to-band tunneling is largely dependent on the concentration of charge carriers on both sides of the junction and the applied bias voltage. Varying the concentration of electrons and holes within reasonable limits shows that the contribution of this mechanism in the total dark current can also be neglected at low bias voltages up to -0.6 V.
The main contribution to the total amount of dark current in reverse bias less than 0.6 V is determined by two mechanisms: the generation in the depletion region and tunneling through traps. The generation-recombination current is also dependent on the concentration of traps. The contribution of other mechanisms is negligible.
The dependence of the dark current on the reverse bias shown in Fig. 15 has a pretty strong inclination that can mean the predominance of the generation-recombination current. That in turn means a high concentration of traps. Unfortunately, we will inevitably obtain high tunneling currents in reverse bias over 0.4V if substituting the concentration of traps provides the observed slope in the calculation. This effect is not observed in the

experimental dependence (curve 1). Varying the other parameters used in the calculations (density, composition, thickness) within the measurement error does not allow to obtain a satisfactory agreement between the experimental and calculated data. Hence, there is at least one other parameter besides the concentration of traps that has a significant influence on the behavior of current-voltage characteristics.

The experimental curves can be reliably described if assuming that a shunt resistance R_{sh} which obeys Ohm's law is parallel connected to the diode. In this case, the total current will be determined by the following expression:

$$I_{sum} = I_{dif} + I_{g-r} + I_{tat} + I_{btb} + \frac{V}{R_{sh}} \quad (11)$$

Calculated current-voltage characteristic (CVC) obtained from the formula (11) (R_{sh} = 1.1 × 10^8 ohms, and N_t = 2.6 × 10^{15} cm^{-3}) corresponds to curve 2 in Figure 15. It is seen that the calculated CVC repeats the experimental with this approach.

The nature of leakage through R_{sh} remains open and requires further study. We assume that the shunting of the p-n junction is due to threading dislocations. The R_0 value was determined directly from the I–V curves, while the A value was evaluated from the measured photocurrent as described in [Gopal et al., 2001]. Figure 16 presents a plot of the R_0A versus cut-off wavelength λ_c in the photodiodes based on HgCdTe/Si(310) heterostructures operating at 77 K. As can be seen, the R_0A product of these photodiodes in a 8–12 μm wavelength range is below the upper values calculated assuming the limitation by thermal generation (curve 1), while significantly exceeding the values determined for a regime limited by the background noise (curve 2) [Rogalski, 2003]. Thus, the obtained data are indicative of a high quality of the material, which is a necessary prerequisite for the development of multielement IRFPAs.

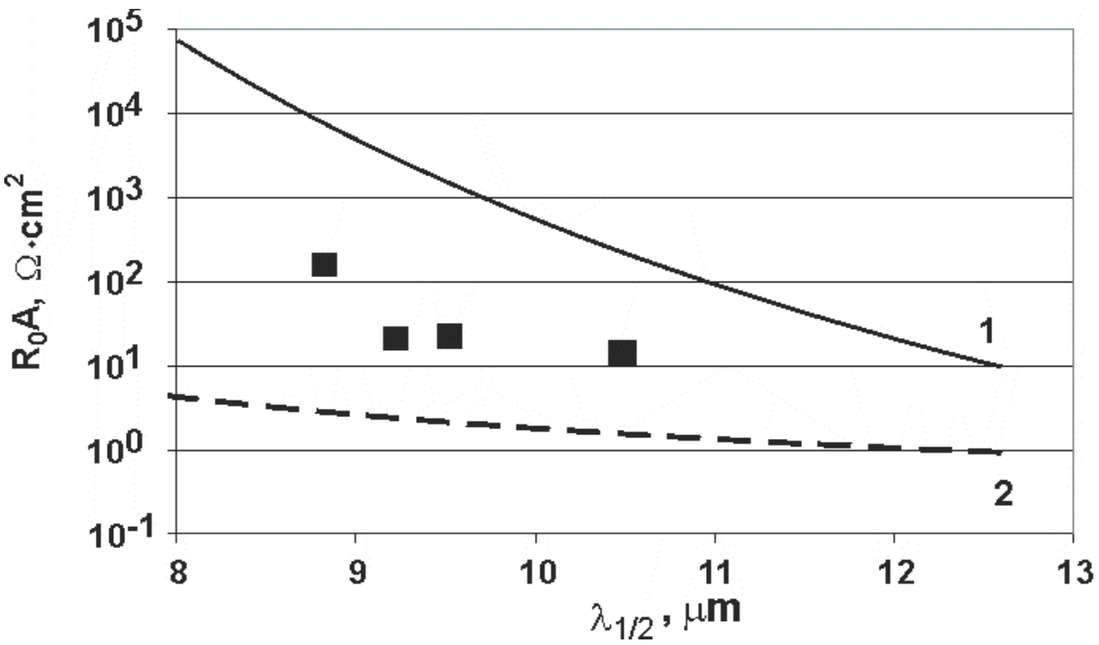

Fig. 16. Dependence of R_0A product on cutoff wavelength for HgCdTe/Si(310)-based photodiodes at 77 K.

6. Properties of HgCdTe/Si(310-based) photodetector arrays

6.1 Mid-wavelength spectral range

Infrared focal-plane arrays of formats of 320 × 256 and 640 × 512 elements for a spectral range of 3–5 μm were fabricated based on photodiode photosensitive elements and a Si multiplexer by the method of hybrid assembly through In bumps, and their characteristics were measured. The temperatures of the sample, background and absolute blackbody were 78, 293, and 501 K, respectively. The measurements were performed in an aperture angle of 56°, the pixel output rate was 2.0 MHz, and the integration time was 640 μs.

The measurements showed that the amount of defect elements in FPAs does not exceed 2.5%, while for the best IR FPAs it is 1%. We assumed that the defect elements are photodiodes with response differing from the average value for more than by 35%, while the threshold irradiation exceeded the average value by a factor of larger than 3. The defect elements are uniformly distributed over the FPA area and do not form clusters in the central part (Fig. 17). The average values and deviation of the volt sensitivity and the noise-equivalent difference in temperature (NEDT) (Fig. 18) are close to the limiting values for these measurement conditions.

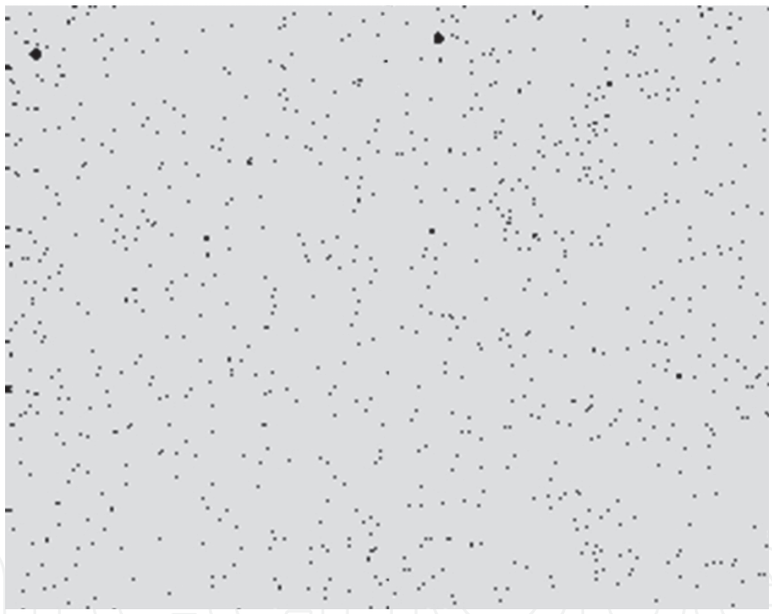

Fig. 17. Topograph of defect elements of 320 × 256 array with c $\lambda_{1/2}$ (77K) = 5.2 μm. The number of defect elements is 0.4% (19 pieces) in the central part of the format 80 × 64 elements

The thermal image obtained using a model of a thermal vision channel based on a photodetector devices of sizes of 320 × 256 and 640 × 512 elements is visually observed in real time, and a characteristic temperature distribution over a human face is observed in the image (Fig. 19).

We studied the effect of temperature cycling from 77 to 300 K on the parameter of the IR FPA ($\lambda_{1/2}$(77 K) = 4.3 μm) based on MBE-grown MCT heteroepitaxial structures on a Si substrate of a size of 320 × 256 elements. The dependences of NEDT and the number of defect elements on the number of the temperature-variation cycles are presented in Fig. 20.

It is seen that, taking into account the measurement error, the average value of NEDT was almost invariable after more than 2500 cycles. The number of defect elements insignificantly increased from 2.25 to 2.9% after the first 400 cycles and was further invariable. The presented results show high stability of the IR FPAs to thermocycling.

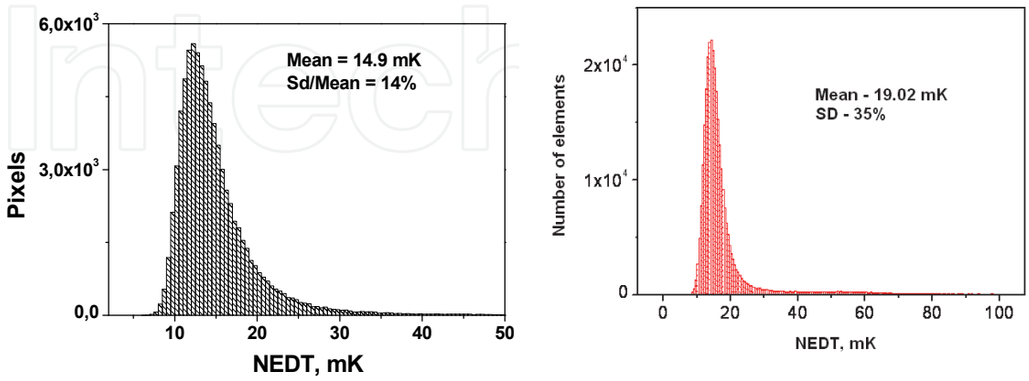

Fig. 18. NEDT histogram for MCT-based 320×256 array with $\lambda_{1/2}$ (77K) = 5.2 μm (a) and 640×512 array with c $\lambda_{1/2}$ (77K) = 4.1 μm (b).

Fig. 19. Thermal image obtained from 640×512 array based on HgCdTe/CdTe/ZnTe/Si(310)

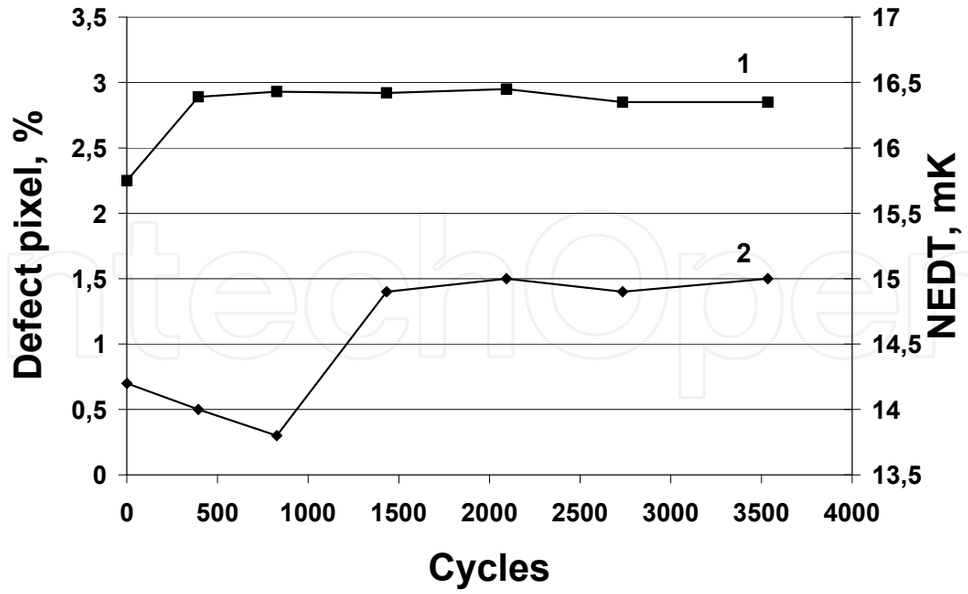

Fig. 20. Dependencies of number of defect elements (1) and NEDT (2) on number of thermocycles from 77 to 300K.

6.2 Long-wavelength spectral range

Using these photosensitive arrays in a hybrid assembly with silicon multiplexers, IRFPAs of the 288 × 4 format were manufactured for a wavelength range of 8–12 μm [λc(77 K) = 9.5 μm].

The IRFPAs of the 288 × 4 format were provided with a silicon multiplexer possessing an original scheme and special design, the distinctive features of which are the fully digital control via parallel and serial interfaces, possibility of deselecting any defect cell, bidirectional scanning of pixels, and possibility of testing the analog parameters.

The multiplexer was manufactured using a commercial 1-μm CMOS technology with two metal and two poly-Si levels [Sizov et al., 2006]. The gate and spacer oxide layers were 40 and 90 nm thick, respectively, with the corresponding specific capacitances of 8.65 ×10^{-4} and 3.8 ×10^{-4} pF/μm². The direct injection was provided by a subdoped n-channel transistor with a threshold voltage of ~0.7 V and a channel length increased to 2.4 μm, which ensured a spread of the bias voltage on the diodes not exceeding 10 mV.

The multiplexer was subdivided into four identical blocks, each of 72 × 4 channels multiplexed to four outputs. The deselect trigger and output device make possible the exclusion of defect diodes and 8-fold variation of the gain. A commutator ensures alteration of the scan direction and direct access to diodes bypassing the TDI tract. A charge-sensitive amplifier provides the charge/voltage conversion and a read-out integrated circuit (ROIC) ensured the gain and storage of analog signals during multiplexing. A charge capacity of the proposed multiplexer is greater than 2.5 pF at a nonlinearity not exceeding 2%.

The performance of this multiplexer with respect to the main functional and electrical characteristics is close to those of a BD TL015-XX-V3 (Sofradir) multiplexer that is employed in Pluton LW 288 × 4 FPAs.

The parameters of IRFPAs were measured at a device temperature of 77 K, a background temperature of 293 K, and a blackbody temperature of 501 K. The measurements were

performed at an aperture angle of 30°, the pixel output rate of 4.0 MHz, and a signal integration time of 18 μs. The tests were carried out with a reject filter having a long-wavelength cut-off 8.0 μm.

Figure 21 shows distributions of the main parameters of IRFPA of the 288 × 4 format based on CMT heteroepitaxial structures grown by MBE on a Si(310) substrate with

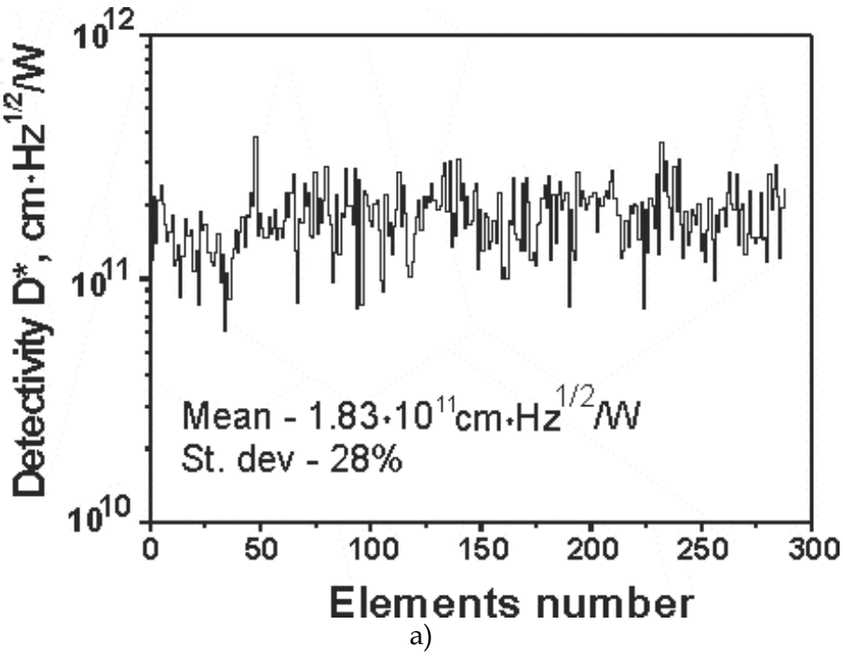

a)

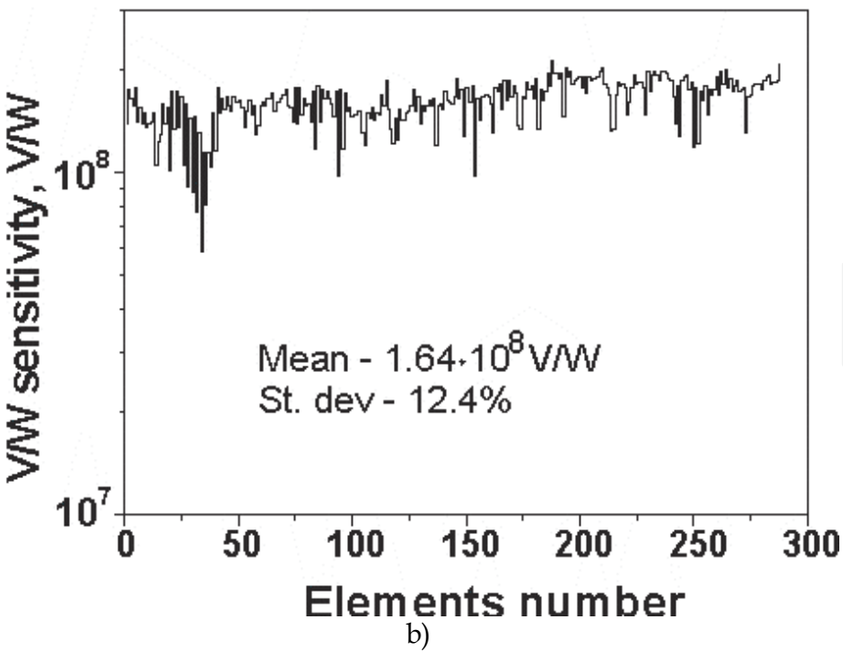

b)

Fig. 21. Topogram of the specific detectivity (a) and voltage sensitivity (b) of 288×4 FPA's channels (λ_c (77K) = 9.5 мкм).

λc(77 K) = 9.5 μm. As can be seen, all 288 channels are photosensitive and their characteristics are not inferior to those of the analogous IRFPAs based on MCT grown on lattice-matched CdZnTe substrates. Indeed, the mean specific detectivity (D*) of the proposed 288 × 4 IRFPA based on HgCdTe/Si(310) heterostructure amounts to 1.83×10^{11} cm*Hz$^{1/2}$/W at a standard deviation of 28%, while the voltage sensitivity is 1.64×10^{8} V/W at a standard deviation of 12.4%. Analogous parameters reported for the IRFPAs based on lattice-matched MCT/CdZnTe heterostructures [Reddy et al., 2008] exceed these values by no more that 5%.

When the linear IRFPAs are employed in technical imaging systems, additional requirements are imposed on the homogeneity of parameters of the elements. In long-wavelength FPAs, channels with a specific detectivity below 5×10^{10} cm*Hz$^{1/2}$ /W are conventionally classified as defect elements. According to this criterion, the presented 288 × 4 IRFPA based on HgCdTe/Si(310) heterostructure has no defect channels, since the minimum specific detectivity is about 6×10^{10} cm*Hz$^{1/2}$/W. Another criterion is the voltage sensitivity, which must fall within ±30% of the mean value. In this respect, the proposed IRFPA has 12 defect channels. However, if the boundaries of admissible variation of the sensitivity are expanded to range from +30% to –60%, then the proposed device is also free of defect channels with respect to sensitivity.

It is believed that the proposed linear IRFPA is characterized by a high stability of parameters with respect to temperature cycling from 77 to 300 K. Indeed, tests that have been previously carried out for 288 × 4 IRFPAs based on HgCdTe/Si(310) heterostructures for a 3–5 μm wavelength range showed that they were highly stable with respect to temperature cycling and their photoelectric parameters remained unchanged upon 1250 cooling/heating cycles.

In conclusion, the present investigation showed that undoped hole-type HgCdTe layers with x =0.23 grown by MBE on Si(310) substrates ensure high photoelectric parameters (limited by background radiation) of IRFPAs of the 288 × 4 format for long-wavelength (8–12 μm) IR spectral range.

7. Conclusion

Investigations of growth processes of MCT MBE on Si(310) substrates for 3rd generation IRFPAs were carried out.

It is shown that the optimization of processes of surface preparation and growth conditions allows to obtain MCT MBE on Si (310) without antiphase domains. Optimization of the growth process and the absence of antiphase boundaries allowed to reduce the density of morphological V-defects to ~ 1000 cm^{-2}.

A technology for the device quality undoped p-type MCT was developed.

It was demonstrated that HgCdTe/CdTe/ZnTe/Si(310) hetrostructures could be used to create reliable, resistant to thermal cycling IRFPAs for the spectral ranges 3-5 and 8-12 μm.

8. References

Aoki T., Chang Y., Badano G., Zhao J., Grein C., Sivananthan S., and David J. Smith., (2003) *J. Electron. Mater.*, Vol. 32, p. 703

Bhan R.K., Dhar V., Chaudhury P.K. et al. (1996) *Appl. Phys. Lett.*, , Vol. 68, No. 17, pp.2453-2454

Blinov V.V., Dvoretsky S.A., Sidorov Yu.G. (1997) Patent of Russian Federation №2071985. Priority from 11.01.1993. Registration 20.01 1997. Bulletin №2 from 20.01.97. (in Russian)

Blinov V.V., Goryaev E.P., Dvoretsky S.A., et al. (1997) Claim for invention № 95102853/25, priority from 01.03.95. Positive solution from 20.08. 1997. (in Russian)

Buldygin A.F., Vdovin A.V., Studenikin S.A., et al. (1996) *Avtometriya*, No. 4, pp.73-76 (in Russian)

Carmody M., Pasko J.G., Edwall D., Piquette E., Kangas M., Freeman S., Arias J., Jacobs R., Mason W., Stoltz A., Chen Y., and Dhar N.K. (2008). Status of (LWIR) HgCdTe-on-Silicon FpA Technology. *J. Electron. Mater.*, Vol. 37(9), p. 1184

Fenner D.B., Biegelsen D.K., Bringans R.D. (1989) Silicon surface passivation by hydrogen termination: A comparative study of preparation methods. *J.Appl. Phys.*, Vol. 66, p.419

Gopal V., Singh S.K. and Mehra R.M. (2001). Excess dark currents in HgCdTe p+-n junction diodes, *Semicond. Sci. Technol.*, Vol. 16, pp. 372-376

Haakenaasen R., Moen T., Colin T., Steen H., and Trosdahl-Iversen L. (2002) Depth and lateral extension of ion milled pn junctions in CdHgTe from electron beam induced current measurements. *J. Appl. Phys.*, Vol. 91, p. 427.

Kern W., Puotinen D.A. (1970) Cleaning solutions based on hydrogen peroxide for use in silicon semiconductor technology. *RCA rev.*, Vol. 31, p. 187

Koestner R. J., Schaake H.F. (1988). Kinetics of molecular-beam epitaxial HgCdTe growth. *J. Vac.Sci.Technol.*, Vol. A 6, No. 4, p. 2834

Kuleshov V.F., Kuharenko Yu.A., Fridrihov S.A., et al. (1985) Spectroscopy and electron diffraction in the study of solid surfaces, Nauka, Moscow (in Russian)

Reddy M., Peterson J.M., Lofgreen D.D., Franklin J.A., Vang T., Smith E.P.G., Wehner J.G.A., Kasai I., Bangs J.W., and Jonson S.M., (2008). MBE Growth of HgCdTe on Large-Area Si and CdZnTe Wafers for SWIR, MWIR and LWIR Detection, *J. Electron. Mater.*, Vol. 37, No. 9, p. 1274.

Remesnik V.G., Mischenko A.M., Mihaylov N.N. (1994) *Invention*, №20. Patent of Russian Federation №2022402, priority from 30.10.94, Bulletin № 20 from 30.10.94. (in Russian)

Rheenen A.D. van, Syversen H., Haakenaasen R., Steen H., Trosdahl-Iversen L. and Lorentzen T. (2006) Temperature dependence of the spectral response of lateral, MBE-grown, ion-milled, planar, HgCdTe photodiodes. *Phys. Scr.* ,Vol. T126, p.101.

Rogalski A. (2003) *Infrared Detectors (Electrocomponent Science Monographs, Volume 10)*, CRC Press

Ryu Y.S., Song B. S., Kang T.W., Kim T.W. (2004) Dependence of the structural and the electrical properties on the Hg/Te flux-rate ratios for $Hg_{0.7}Cd_{0.3}Te$ epilayers grown on CdTe buffer layers, *J. Mater. Sci.*, Vol. 39, p. 1147

Sabinina I.V., Gutakovsky A.K., Sidorov Yu.G., Latyshev A.V. (2005) Nature of V-shaped defects in HgCdTe epilayers grown by molecular beam epitaxy. *J. Crystal Growth*, Vol. 274, p. 339

Schoolar R., Price S., Rosbeck J. (1992). *J. Vac. Sci. Technol.*, Vol. *B* 10, pp. 1507–1514

Sheldon P., Jones K.M., Al-Jassim M.M., Yacobi B.G. (1988) Dislocation density reduction through annigilation in lattice-mismatched semiconductors grown by MBE. *J.Appl. Phys.*, Vol.63, No.11, pp.5609-5611.

Sidorov Yu.G., Varavin V.S., Dvoretsky S.A. et al. (1996) *In Growth of Crystals*, Vol.20, pp.35-45.

Sidorov Yu.G., S.A. Dvoretsky, Mihaylov N.N., Yakushev M.V., Varavin V.S., Antsiferov A.P. (2000). Molecular beam epitaxy of narrow-band materials CdHgTe. Equipment and technology. *Opticheskiy zhournal*, Vol. 67, No.1, p. 39 (in Russian)

Sidorov Yu.G., S.A. Dvoretsky, Mihaylov N.N., Varavin V.S., (2001) Physico-chemical and technical basis of molecular-beam epitaxy of $Cd_xHg_{1-x}Te$. In: *Infrared focal plane arrays*, Nauka, Novosibirsk (in Russian)

Sivananthan S., Chu X., Reno J., Faurie J.P. (1986). *J. Appl. Phys.*, Vol. 60 (4), p. 1359

Sizov F. F., Vasil'ev V.V., Suslyakov A.O., Reva V.P., Golenkov A.G. (2006) 4×288 Readouts and FPAs Propeties, *Optoelectron review*, Vol. 14., pp. 67–74.

Tashikawa M., Yamaguchi M. (1990) Film thickness dependence of dislocation density reduction in GaAs on Si substrates. *Appl. Phys. Lett.*, Vol. 56, No.5, pp.484-486.

Vasiliev V. V., Klimenko A.G., Marchishin I.V., Ovsyuk V. N., Talipov N. Kh., Zakhar'yash T.I, Golenkov A. G., Derkach Yu. P., Reva V. P., Sizov F. F., Zabudsky V. V. (2004) MCT heteroepitaxial 4×288 FPA. *Infrared Physics&Technology*, Vol. 44, pp. 13-23,

Vilela M.F., Buell A.A., Newton M.D., Venzor G.M., Childs A.C., Peterson J.M., Franklin J.J., Bornfreund R.E., Radford W.A., and Johnson S.M. (2005) Control and Growth of Middle Wave Infrared (MWIR) HgCdTe on Si by Molecular Beam Epitaxy. *J. Electron. Mater.*, Vol. 34, No. 6, p.898.

Voitsehovsky A.V., Denisov Yu.A., Kohanenko A.P., et al. (1996) *Avtometriya*, Vol. 4, pp..51-58 (in Russian)

Wang C.C., Me Farlane S.H. *(*1976) Crystal growth and defect chracterization of heteroepitaxial III-V semiconductor films, *Thin Solid Films*, Vol. 31, No. 3, p. 323-332

Yakushev M.V., Babenko A.A., Sidorov Yu.G. (2009) Effect of substrate orientation on the growth conditions of HgTe films grown by molecular beam epitaxy, *Neorganicheskie materialy*, Vol. 45, No. 1, p. 15 (in Russian)

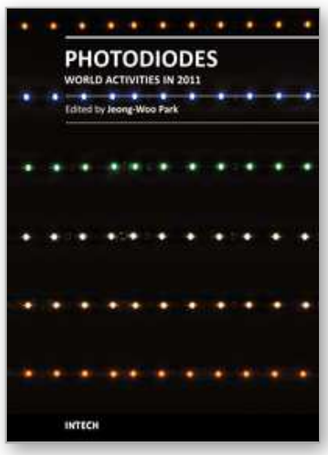

Photodiodes - World Activities in 2011

Edited by Prof. Jeong Woo Park

ISBN 978-953-307-530-3
Hard cover, 400 pages
Publisher InTech
Published online 29, July, 2011
Published in print edition July, 2011

Photodiodes or photodetectors are in one boat with our human race. Efforts of people in related fields are contained in this book. This book would be valuable to those who want to obtain knowledge and inspiration in the related area.

How to reference

In order to correctly reference this scholarly work, feel free to copy and paste the following:

Maxim Yakushev, Vasily. Varavin, Vladimir Vasilyev, Sergey Dvoretsky, Irina Sabinina,Yuri. Sidorov, Aleksandr Sorochkin and Aleksandr Aseev (2011). HgCdTe Heterostructures Grown by MBE on Si(310) for Infrared Photodetectors, Photodiodes - World Activities in 2011, Prof. Jeong Woo Park (Ed.), ISBN: 978-953-307-530-3, InTech, Available from: http://www.intechopen.com/books/photodiodes-world-activities-in-2011/hgcdte-heterostructures-grown-by-mbe-on-si-310-for-infrared-photodetectors

INTECH
open science | open minds

InTech Europe
University Campus STeP Ri
Slavka Krautzeka 83/A
51000 Rijeka, Croatia
Phone: +385 (51) 770 447
Fax: +385 (51) 686 166
www.intechopen.com

InTech China
Unit 405, Office Block, Hotel Equatorial Shanghai
No.65, Yan An Road (West), Shanghai, 200040, China
中国上海市延安西路65号上海国际贵都大饭店办公楼405单元
Phone: +86-21-62489820
Fax: +86-21-62489821

IntechOpen